



RESEARCH MEMORANDUM

A FREE-FLIGHT INVESTIGATION OF THE DRAG COEFFICIENTS
OF TWO SINGLE-ENGINE SUPERSONIC INTERCEPTOR
CONFIGURATIONS FROM MACH NUMBER 0.8 TO
1.90 TO DETERMINE THE EFFECT OF
INLET AND ENGINE LOCATIONS

By Joseph H. Judd

Langley Aeronautical Laboratory
Langley Field, Va.

NATIONAL ADVISORY COMMITTEE
FOR AERONAUTICS
WASHINGTON

September 28, 1955
Declassified August 14, 1958

NATIONAL ADVISORY COMMITTEE FOR AERONAUTICS

RESEARCH MEMORANDUM

A FREE-FLIGHT INVESTIGATION OF THE DRAG COEFFICIENTS
OF TWO SINGLE-ENGINE SUPERSONIC INTERCEPTOR
CONFIGURATIONS FROM MACH NUMBER 0.8 TO
1.90 TO DETERMINE THE EFFECT OF
INLET AND ENGINE LOCATIONS

By Joseph H. Judd

SUMMARY

Flight tests were made of two single-engine supersonic interceptor configurations and an idealized model, all with 52.5° sweptback wings and tail surfaces, NACA 65A004 airfoil sections, taper ratios of 0.2 and aspect ratios of 3.0. The first interceptor configuration had a half-conical scoop inlet under the fuselage and was designed for engine installation in the aft part of the fuselage; the second configuration had a full-conical spike inlet mounted near the nose of the fuselage and in line with the design engine location, which was in a pod on the underside of the fuselage. The Mach number range of the tests was from 0.8 to 1.90 and the Reynolds number range was from 3.8×10^6 to 16×10^6 . Bodies of revolution with the same cross-sectional areas as the two interceptor configurations were also test flown.

At supersonic speeds, from a Mach number of 1.3 to 1.90, the drag coefficients were approximately 0.025. At subsonic speeds, the interceptor configuration with the half-conical scoop under the fuselage has a lower drag coefficient (0.0105) than the configuration with the engine pod (0.0150).

Total-pressure recovery and mass-flow ratio for the half-conical spike inlet were approximately the same as computed by cone and shock-wave relationships for a circular inlet. However, separation of the inlet flow adjacent to the fuselage of the interceptor with the engine pod reduced total-pressure recovery by 3 percent and mass-flow ratio by about 0.065.

INTRODUCTION

Recent results (ref. 1) in the study of drag have indicated that component interference drag has been a major source of high airplane drag at transonic and low supersonic speeds. Such interference drag naturally depends on the nature of the entire configuration and probably on the cross-sectional-area distribution of the configuration. It was deemed important, therefore, that, when the Pilotless Aircraft Research Division conducted an investigation of the effect of engine and inlet installation on drag, complete airplane configurations should be tested. The information presented herein concerns the drag coefficients of two single-engine supersonic interceptors on which the inlet type, inlet location, and engine location were varied.

The National Advisory Committee for Aeronautics has conducted tests in which the drag coefficients of wing-body combinations (refs. 2 and 3, for example) have been measured. Similarly, the subject of inlet design has been investigated from the standpoint of inlet recovery and drag, as exemplified by reference 4 for scoop inlets and references 5 and 6 for nose inlets. The present investigation was made to determine the magnitude of drag-coefficient increase which can be attributed to engine installation.

In order to provide a measure of practicality to these tests, a preliminary design of a Mach number 2.0 single-engine interceptor was made. The total plan-form wing area of the airplane was 276.5 square feet. Table I presents some of the airplane parameters. In order to check on the useful volume of the airplane, equipment from a present-day interceptor was laid out on the drawing of the configuration. A 52.5° sweptback wing of aspect ratio 3.0, taper ratio 0.2, and NACA 65A004 airfoil section was selected since this wing combined the properties of low supersonic drag coefficients and good lift efficiency at subsonic cruising speeds. It was realized that changes in inlet type and location and engine location would change the fuselage radically in appearance and modify the wing roots to some extent. Thus, in order to provide some measure of similarity between configurations, the wing size and tail size were kept the same.

The first interceptor configuration tested had a half-conical spike inlet under the fuselage at the wing leading edge, and the fuselage was designed for an aft engine location. A 0.104-scale model of this configuration was test flown. The second interceptor configuration utilized a conical spike inlet under the nose of the fuselage and in line with the design engine location which was in a pod contiguous to the underside of the fuselage. A 0.118-scale model of this configuration was test flown.

In order to obtain high supersonic speed, the airplane must have a low supersonic drag coefficient. For this reason, all components were made as slender as possible. Although the value of the transonic area rule was appreciated, it was felt that a drag penalty would be assessed at the design Mach number of 2.0 if any radical shape modifications were made to satisfy requirements at a Mach number of 1.0. Data of reference 2 have substantiated this viewpoint. In order to satisfy both conditions, the components were arranged in such a manner as to provide a smooth cross-sectional-area distribution at Mach number 1.0.

The flight models in these tests were boosted by a single large rocket under the fuselage. An exploratory separation model was flown to determine model loads due to separation of the model and booster. This model was similar to the scoop model except that the inlet was faired to the nose and the canopy was omitted. Although the information on separation characteristics is scanty, it is included as an appendix to provide an indication of the loads that can occur on a high-speed aircraft when launched by a large underslung-type booster to supersonic speeds.

All tests were made at the Langley Pilotless Aircraft Research Station at Wallops Island, Va. Rocket-propelled models of the airplane configurations were flown and 1/5-scale bodies with the same cross-sectional-area distributions as the interceptor configurations were flight tested with a helium gun. The Mach number range of these tests was from 0.8 to 1.95, and the Reynolds number range was from 3.8×10^6 to 16×10^6 .

SYMBOLS

A	cross-sectional area, sq ft
A_{max}	maximum total fuselage cross-sectional area, sq ft
A_e	duct-exit area, sq ft
A_1	inlet minimum area, sq ft
A_i	inlet capture area, sq ft
C_D	drag coefficient based on total wing area
C_{Di}	internal drag coefficient based on total wing area

C_N	normal-force coefficient based on total wing area
H_D	inlet total pressure, lb/sq ft
H_O	free-stream total pressure, lb/sq ft
l	model length, ft
m	inlet mass flow, slugs/sec
m_O	free-stream mass flow across A_1 , slugs/sec
M_e	duct-exit Mach number
M	free-stream Mach number
p_e	duct-exit static pressure, lb/sq ft
p_O	free-stream static pressure, lb/sq ft
r	radius of equivalent body of revolution, ft
R	Reynolds number based on mean aerodynamic chord or scale mean aerodynamic chord for equivalent bodies of revolution
S	wing area, sq ft
x	distance from nose of fuselage, ft
β	vertical camera-plane angle
γ	horizontal camera-plane angle
θ	pitch-attitude angle
θ'	camera flight-path angle
ϕ	roll angle

MODELS

Three-view drawings and photographs of the three rocket-propelled configurations are presented in figures 1 and 2. All models had wing

and tail sections of 52.5° sweepback at the quarter chord, aspect ratios of 3.0, taper ratios of 0.2, and NACA 65A004 airfoil sections. The interceptor configuration with the half-conical spike inlet under the fuselage will hereinafter be referred to as model 1. The interceptor configuration with the engine in a pod under the fuselage will be referred to as model 2, and the idealized model with no duct or canopy, model 3.

Table II(a) presents the general physical characteristics of model 1. The scoop and engine location on model 1 virtually dictated the fuselage shape; ordinates of this shape are given in table III(a). Basically, the fuselage started out as a parabolic body with a forebody fineness ratio of 6.0 and with the addition of the scoop deepened into an oval fuselage. The aircraft fuselage would have ended at reference fuselage station 75.00 but the fuselage of the model was extended to station 79.00 to minimize the base area. The inlet was a half-conical spike inlet with the floor shaped to fit the underside of the fuselage and was located at fuselage station 28.00. The general view of the inlet on the aircraft is shown in figure 2(a), and drawings and photographs of the inlet are shown in figures 3(a) and 4(a). External compression was accomplished by a 25° half-angle cone. A boundary-layer bypass was made by putting a metal sheet from the point of the cone to the cowl. A wedge of 40° total angle under the boundary-layer splitter plate diverted the flow to each side of the fuselage. The height of the plate was 0.40 inch, corresponding to the calculated boundary-layer height at $M = 1.0$. The inlet capture area was 0.0484 square foot and the inlet minimum area was 0.0358 square foot. There was no internal contraction at the inlet. The duct expanded to a full-round section and then contracted to the exit which had an area of 0.0400 square foot.

The general physical characteristics of model 2 are presented in table II(b). Because of difficulties involved in telemeter installation, model 2 was made larger than model 1. Although the fuselage shape of model 1 was determined by scoop and engine installation, the fuselage shape of model 2 was evolved to get a smooth fuselage-pod area distribution which would fair with areas of wing and tail. Fuselage ordinates are given in table III(b). The inlet was a 25° half-angle conical inlet with no internal contraction ratio and was located at fuselage station 12.893. The inlet cowl was located 0.18 inch from the fuselage surface, which corresponds to the boundary-layer height at $M = 1.0$. The general location and installation of the inlet are shown in figure 2(c). Inlet and duct details are given in figures 3(b) and 4(b). A straight duct was used in this model, with a contracting nozzle at the exit. The inlet capture area was 0.0612 square foot, and the inlet minimum area was 0.0457 square foot. There was no internal contraction at the inlet. The duct exit was located at fuselage station 64.024 and had an area of 0.0562 square foot.

Model 3 was an idealized version of interceptor configuration 1 and had no canopy or duct. Since the purpose of this model was to determine loads on the model at separation of the model and booster, the wing and tail surfaces were left in an "as cast" condition. This condition caused the surfaces to be much rougher than either of the interceptor wings. The geometric relationship between wing and tail surfaces and sizes were the same as for model 1 and are tabulated in table II(c). Fuselage ordinates for model 3 are given in table III(c). Three-view drawings and photographs of this model are presented in figures 1(c) and 2(e).

The booster used in these tests was a 6.25-inch Deacon rocket motor. The fins were tapered plates with wedge leading edges. A drawing of the booster for model 3 is given in figure 5, a photograph of the booster with support struts down is given in figure 6, and a photograph of model 3 with the booster on model launcher is shown in figure 7. A faired nose for the booster was used to reduce the magnitude of the nose pressure field at separation. The forward model supports were brought parallel by aerodynamic forces to the plane of the model wings. Weight and center-of-gravity positions for model 3 and booster are:

Weight of model, lb	60.38
Weight of booster (empty), lb	95.00
Center of gravity of model, in.	40.07
Center of gravity of booster, in.	79.43

One-fifth-scale bodies of revolution with the same cross-sectional-area distribution as the interceptor models were constructed of magnesium. Figure 8 presents the area distributions of the interceptor configurations. Three fins of hexagonal airfoil section were used for stability. The cross-sectional-area distributions of the bodies of revolution, including the stabilizing fins, were the same as the bodies shown in figure 8. Photographs of these models are shown in figure 9.

TESTS AND INSTRUMENTATION

Flight Tests of Interceptor Models

The interceptor models were launched from a mobile launcher. Figure 7 shows model 3 with booster on the launcher prior to firing. A single ABL Deacon rocket motor propelled the combination to the peak Mach number. The information presented in this report was obtained during the decelerating flight after separation of the model from the booster. The range of Reynolds number for the rocket-propelled models, based on the wing mean aerodynamic chord, and the Mach number are

presented in figure 10. The Reynolds number range for the helium-gun models, based on body length, was from 35×10^6 to 47×10^6 .

Data for the flight tests were obtained by use of telemeter, CW Doppler velocimeter, tracking radar, tracking cameras, and radiosonde. The radiosonde gave a survey of the atmospheric conditions over the altitude range covered by the models. In addition, the velocity and direction of the winds were obtained from radiosonde data. All model velocities were corrected for wind velocities.

Each of the interceptor models carried a telemeter unit to transmit flight data to ground receiving stations. Models 1 and 2 employed four channels which transmitted longitudinal and normal accelerations, duct-exit static pressure, and differential total pressure between nose and duct inlet. Since model 3 was flown to obtain separation characteristics and separation loads on the models, the quantities measured were normal and longitudinal accelerations.

The drag coefficients were obtained by differentiation of the model velocity and by use of atmospheric data from the radiosonde. In addition, the drag coefficient was computed from the longitudinal acceleration obtained from the accelerometer. In addition to providing a check on the accuracy of data, the drag data from the accelerometer gave better definition of the drag-coefficient curves where rapid changes of drag coefficient occurred. The normal-force coefficient was obtained by using the normal acceleration from the accelerometer, the CW Doppler velocity, and the radiosonde data. A differential pressure cell measured the difference between nose total pressure and inlet total pressure at a point near the fuselage. Nose total pressure is computed from the relationship of radiosonde data, CW Doppler velocity, and normal-shock theory. The exit static pressure of the duct was used to compute the inlet mass-flow ratio, internal drag coefficient, and exit total-pressure recovery:

$$\frac{m}{m_0} = \frac{P_e}{P_0} \frac{M_e}{M} \frac{(1 + .2M_e^2)^{1/2}}{(1 + .2M^2)^{1/2}} \frac{A_e}{A_1}$$

$$C_{D_i} = 2 \frac{m}{m_0} \frac{A_1}{S} \left[1 - \frac{M_e}{M} \frac{(1 + .2M^2)^{1/2}}{(1 + .2M_e^2)^{1/2}} \right] - \frac{P_e - P_0}{q} \frac{A_e}{S}$$

When sonic flow exists at the exit, the foregoing equations can be used to compute the mass-flow ratio and internal drag coefficients since enough quantities are known. However, when the exit is no longer choked, the mass-flow ratio and internal drag coefficient cannot be computed

directly. For the range from Mach number 0.8 to that at which the exit chokes, the variation of mass-flow ratio is assumed by extrapolating the supersonic m/m_0 curve by considering the relationship to the theoretical m/m_0 curve (refs. 5 and 7). Then the exit Mach number can be computed by using the continuity equation. If this value of exit Mach number is substituted into the formula for C_{D1} , the values of internal drag coefficient can be computed.

The external drag coefficients of models 1 and 2 were obtained by subtracting the internal drag coefficients from the total drag coefficients.

Helium-Gun Tests of Bodies of Revolution

The bodies of revolution which had the cross-sectional-area distributions of models 1 and 2 were test fired from a helium gun as described in reference 8. Data for these flight tests were obtained during decelerating flight. A CW Doppler velocimeter, tracking radar, and radiosonde furnished the data. The model drag coefficients were computed by differentiation of the model velocity as obtained from the velocimeter and by use of atmospheric data from the radiosonde.

ACCURACY

The basic accuracy of drag coefficients obtained from differentiation of model velocities obtained from the velocimeter has been qualitatively established in reference 9. The source of error consists of model dissimilarities due to construction and finish, instrumentation errors of the velocimeter, tracking radar, and radiosonde, and, finally, the error in reading and computing of data. On the basis of statistical data compiled by the Instrument Research Division of the Langley Laboratory, the maximum telemeter error is within ± 2 percent of the full-scale range, whereas the probable error is within ± 1 percent of the full-scale range of the instruments. Thus, the probable errors for the models are within the values tabulated as follows:

Probable errors in -								
M	ΔM	Total ΔC_D	$\Delta H/H$	Model 1 ΔC_N	Model 2 ΔC_N	Model 3 ΔC_N	ΔC_{D1}	External ΔC_D
0.9	± 0.005	± 0.0007	± 0.0364	± 0.0009	± 0.0023	± 0.0098	± 0.0008	± 0.0011
1.1	± 0.005	± 0.0007	± 0.0333	± 0.0006	± 0.0016	± 0.0058	± 0.0007	± 0.0010
1.8	± 0.005	± 0.0007	± 0.0198	± 0.0003	± 0.0004	± 0.0018	± 0.0001	± 0.0007

The accuracy of measurements made on models propelled from the helium gun has been determined by experience gained on previous tests. The Mach number error is within ± 0.005 , and the error in drag coefficient is within ± 0.0008 .

Telemeter accuracy of model 3 during the separation period is tabulated in the preceding table. The accuracy of the model and booster angles cannot be established since the roll angle of the model can be only approximately determined.

RESULTS AND DISCUSSION

Configuration Drag

The basic test data for the interceptor configurations are presented in figures 11 and 12. These include the total and internal drag coefficients and normal-force coefficients. Zero-lift drag coefficients for the bodies of revolution with cross-sectional-area distributions equivalent to the interceptor configurations are presented in figure 13. The external drag coefficients of the interceptor configurations, model 1 and model 2, were obtained by subtracting the internal drag coefficient from the total-drag coefficient. The external drag coefficients of models 1 and 2 are plotted in figure 14 against Mach number, together with the drag of an indented body of revolution with the same wing plan form and the cross-sectional-area distribution of a parabolic body (ref. 3).

The subsonic drag coefficient of model 2 (0.0145) was approximately 38 percent greater than that of either model 1 (0.0105), or the simple wing-body combination. The ratio of exposed area to wing area of model 1 was 4.905 as compared with 4.780 for model 2; the drag coefficient of model 1, based on surface area, was 0.00215 as compared with 0.00315 for model 2. Although reference 10 indicates that some differences in subsonic drag coefficient are caused by differences in wing finish, the calculated turbulent skin-friction drag coefficient for model 2 was 0.01336 when values of average turbulent skin-friction coefficients from reference 11 were used. The main part of the difference in subsonic drag level was probably due to flow separation over the engine-pod and fuselage-pod intersection. Reference 12 shows that unfavorable junctures can cause appreciable drag increases throughout the Mach number range.

Figure 15 shows a comparison of the pressure-drag rise of the interceptor configurations, bodies of revolution with similar cross-sectional-area distribution, and a 52.5° sweptback wing on an indented body (ref. 3). These drag curves show that model 1 has a larger drag rise from subsonic to supersonic speeds than the other configurations.

This extra pressure-drag rise is attributed to the location of the inlet with respect to the components of the airplane.

The total drag coefficients and normal-force coefficients for the idealized configuration are plotted in figure 16. Because of the roughness of wing and tail surfaces, which were left in an "as cast" condition, the only drag comparison that can be made is the drag rise from subsonic to supersonic speeds. The pressure-drag rise of the idealized configuration, model 3, is compared with that of model 1 in figure 17. This comparison furnishes additional evidence that the drag rise of model 1 is high, although addition of the canopy would tend to raise the pressure drag of model 3 by 0.00178 at a Mach number of 1.15 and by 0.00285 at a Mach number of 1.45 (ref. 13). Offsetting this increase in drag are values of base drag coefficient for model 3. Values of the base drag coefficient for model 3 were computed from references 14 and 15. These coefficients are plotted on figure 17.

The supersonic drag coefficients for models 1 and 2 are approximately 0.025 for Mach numbers from 1.30 to 1.90. These values are low enough so that either configuration can fly at Mach number of 2.0 at a 60,000-foot altitude, with the contemporary engine used in initial design calculations.

Trim Lift Coefficients

The variation of normal-force coefficient with Mach number for the interceptor configurations is given in figures 11 and 12, and that of the idealized model, in figure 16. The magnitude of normal-force coefficients is low enough that, over the Mach number range for which data are presented, the values of drag coefficients discussed in the preceding section may be considered zero-lift data. Furthermore, these normal-force coefficients can be called the trim lift coefficients at an elevator setting of 0° . Models 2 and 3 exhibit the same general characteristics over the Mach number range, that is, a nose-down trim at subsonic and transonic speeds and a nose-up trim at supersonic speeds. Model 1 trims at positive angles of attack except near Mach number 1.0. Although the normal accelerometer exceeded the range from Mach number 1.33 to the peak Mach number, it is apparent that model 1 shows a greater trim angle than do models 2 and 3. Because of a possibly higher normal-force coefficient, the drag of model 1 above Mach number 1.33 may be lower than the drag shown in figures 14 and 15. The increase in trim was apparently due to the location of the scoop inlet. The positive pressure field caused by the inlet affects the leading portion of the wing by causing a nose-up trim tendency.

The change in trim caused by jet flow acting on the tail of model 2 was computed using data from reference 16 and calculating the

duct-exit total pressure at booster separation altitude. Calculations indicated that a nose-down change in trim lift coefficient of 0.076 should occur at free-stream Mach number 2.0 between jet-on and jet-off flight conditions. From figure 12, it can be seen that a negative trend in the trim lift coefficient occurs after Mach number 1.65; this trend increases with Mach number. Up to this Mach number, the pressure ratio of the jet is not great enough to affect the trim of the configuration appreciably.

Inlet Characteristics

Data on the total-pressure recovery of the inlets are presented in figure 18. The total-pressure tubes for models 1 and 2 were located 0.25 inch from the inlet wall adjacent to the fuselage and had a twofold purpose. The information can indicate inlet recovery or tell whether flow separation occurs along the wall adjacent to the fuselage. From figure 18 it can be seen that theoretical recovery, calculated for a circular-conical spike inlet by cone and shock-wave relationships, existed in the inlet of model 1 and that no noticeable separation occurred. Model 2 exhibits a slightly lower value of total-pressure recovery, and the irregularity of the H_D/H_0 curve of figure 18(b) indicates that separation occurred along the wall adjacent to the fuselage. This separation is probably caused by the shock from the diffuser cone acting on the fuselage boundary layer.

The mass-flow ratio of the inlets is given in figure 19. Model 1 agrees with the theoretical values computed from reference 7. The slight discrepancy could be due to boundary-layer growth on the boundary-layer splitter plate. This mass-flow-ratio data and data from the inlet total-pressure tube show that no separation occurred. The measured value of mass-flow ratio for model 2 is significantly lower than computed values. This checks the information from the total-pressure tube that a significant amount of separation occurs at the inlet. It is obvious then that a boundary-layer splitter plate is needed on model 2, or that a type of inlet better able to prevent shock boundary-layer interaction should be used.

CONCLUSIONS

Flight tests for a Mach number range from 0.8 to 1.90 were made for two single-engine interceptor configurations with 52.5° sweptback wings and tail surfaces. A half-conical scoop inlet was located under the fuselage of the first interceptor, and a full-conical scoop inlet was located under the fuselage nose ahead of the engine pod on the

second interceptor. An idealized model of the first configuration with no canopy and with the scoop faired to the nose of the fuselage was also flight tested. The Reynolds number range of these tests was from 3.8×10^6 to 16×10^6 . In addition, bodies of revolution having the same cross-sectional-area distributions as the two interceptors were test flown. The following statements summarize the results of the tests:

1. The supersonic drag coefficients of all the configurations were approximately the same and had a value of 0.025. However, the scoop inlet of the first configuration provided a higher pressure-drag rise at supersonic speeds, and the inlet and pod installation of the second configuration provided a higher subsonic drag than did a parabolic body with the same wing.
2. A nose-up trim tendency appeared for the model with the half-conical scoop inlet that was greater than for the other aircraft models, probably because of the action of the inlet flow field on the leading portions of the wing.
3. The half-conical scoop inlet had values of total-pressure ratio and mass-flow ratio that corresponded to theoretical values computed from cone and shock-wave relationships for circular spike inlets. Because of separation at the inlet, the full-conical spike inlet had consistently lower values of mass-flow ratio than did the half-conical scoop inlet.

Langley Aeronautical Laboratory,
National Advisory Committee for Aeronautics,
Langley Field, Va., June 20, 1955.

APPENDIX

SEPARATION CHARACTERISTICS OF A MODEL FROM A LARGE
UNDERSLUNG BOOSTER AT MACH NUMBER 1.95

The separation characteristics of the model and the booster were determined from motion pictures taken during the flight, telemeter data, and tracking radar. The tracking radar locates the model and booster in space, and the photographs of the model give changes in model and booster angles. The true model attitude angles were obtained by correcting the projected flight-path angles from the photographs for the angle between the model plane and the image planes, and the roll angle of the model. Figure 20 shows a schematic drawing of the spatial relationship between model and camera. The correction to the flight-path angle obtained from the camera is given by the following expression:

$$\theta = \tan^{-1} \frac{\tan \theta' \cos(90^\circ - \gamma)}{\cos \beta \cos \phi}$$

In the computations, the average distances, camera-plane angles γ and β , and roll angle ϕ were used during the separation time. The loads on the model were obtained from telemeter data.

The separation characteristics to be discussed are those of the model in the flow field of the booster. Figure 21 gives a graphical presentation of model and booster position relative to each other during this portion of flight. The model and booster separate smoothly and follow slightly divergent flight paths. Separation occurred at a Mach number of 1.95, an altitude of 2,700 feet, and q of 5,550 pounds per square foot. The change in model normal-force coefficients is also presented in figure 21. After separation, the model and booster flew smoothly along until the flow field of the booster nose hit the tail of the model. Then the model, which had a wing loading of 20 pounds per square foot, experienced normal accelerations at $\pm 35g$.

Although at present the subject of model-booster separation is of limited interest, future work on high-speed aircraft which utilize large boosters will result in interest in this type of booster system. The booster used in these tests was relatively long and slender; this should minimize separation loads. If this type booster were used to boost the design interceptor configuration outlined in this paper to the same Mach number and altitude, loads of $\pm 7g$ would occur. These loads are under usual design loads, but the pilot would be very uncomfortable.

REFERENCES

1. Whitcomb, Richard T.: Recent Results Pertaining to the Application of the "Area Rule." NACA RM L53I15a, 1953.
2. Morrow, John D., and Nelson, Robert L.: Large-Scale Flight Measurements of Zero-Lift Drag of 10 Wing-Body Configurations at Mach Numbers From 0.8 to 1.6. NACA RM L52D18a, 1953.
3. Hoffman, Sherwood: A Flight Investigation of the Transonic Area Rule for a 52.5° Sweptback Wing-Body Configuration at Mach Numbers Between 0.8 to 1.6. NACA RM L54H13a, 1954.
4. Weinstein, Maynard I.: Performance of Supersonic Scoop Inlets. NACA RM E52A22, 1952.
5. Sears, R. I., Merlet, C. F., and Putland, L. W.: Flight Determination of Drag of Normal-Shock Nose Inlets With Various Cowling Profiles at Mach Numbers From 0.9 to 1.5. NACA RM L53I25a, 1953.
6. Merlet, Charles F., and Putland, Leonard W.: Flight Determination of the Drag of Conical-Shock Nose Inlets With Various Cowling Shapes and Axial Positions of the Center Body at Mach Numbers From 0.8 to 2.0. NACA RM L54G21a, 1954.
7. Fraenkel, L. E.: Some Curves for Use in Calculations of the Performance of Conical Centerbody Intakes at Supersonic Speeds and at Full Mass Flow. Tech. Note No. Aero. 2135, British R.A.E., Dec. 1951.
8. Hall, James Rudyard: Comparison of Free-Flight Measurements of the Zero-Lift Drag Rise of Six Airplane Configurations and Their Equivalent Bodies of Revolution at Transonic Speeds. NACA RM L53J21a, 1954.
9. Pepper, William B., Jr., and Hoffman, Sherwood: Transonic Flight Tests To Compare the Zero-Lift Drag of Underslung and Symmetrical Nacelles Varied Chordwise at 40 Percent Semispan of a 45° Sweptback, Tapered Wing. NACA RM L50G17a, 1950.
10. Bingham, Gene J., and Braslow, Albert L.: Subsonic Investigation of Effects of Body Indentation on Zero-Lift Drag Characteristics of a 45° Sweptback Wing-Body Combination With Natural and Fixed Boundary-Layer Transition Through a Range of Reynolds Number From 1×10^6 to 8×10^6 . NACA RM L54B18a, 1954.

11. Van Driest, E. R.: Turbulent Boundary Layer in Compressible Fluids. Jour. Aero. Sci., vol. 18, no. 3, Mar. 1951, pp. 145-160, 216.
12. Judd, Joseph H.: Flight Investigation of Engine Nacelles and Wing Vertical Position on the Drag of a Delta-Wing Airplane Configuration From Mach Number 0.8 to 2.0. NACA RM L53L21, 1954.
13. Welsh, Clement J., and Morrow, John D.: Flight Investigation at Mach Numbers From 0.8 to 1.5 of the Drag of a Canopy Located at Two Positions on a Parabolic Body of Revolution. NACA RM L51A29, 1951.
14. Fraenkel, L. E.: Calculations of the Pressure Distributions and Boundary Layer Development on a Body of Revolution With Various Parabolic Afterbodies at Supersonic Speeds. Rep. No. Aero. 2482, British R.A.E., Feb. 1953.
15. Love, Eugene S.: The Base Pressure at Supersonic Speeds on Two-Dimensional Airfoils and Bodies of Revolution (With and Without Fins) Having Turbulent Boundary Layers. NACA RM L53C02, 1953.
16. Bressette, Walter E.: Investigation of the Jet Effects on a Flat Surface Downstream of the Exit of a Simulated Turbojet Nacelle at a Free-Stream Mach Number of 2.02. NACA RM L54E05a, 1954.

TABLE I
INTERCEPTOR DESIGN PARAMETERS

Total empty weight, lb	14,185
Total useful load, lb	13,077
Take-off gross weight, lb	27,262
Wing loading at take-off, lb/sq ft	98.60
Altitude, ft	50,000
Level-flight drag coefficient at $M = 2.0$	0.032
Thrust coefficient ($4,000^{\circ}$ F afterburner)	0.047

TABLE II
INTERCEPTOR PHYSICAL DIMENSIONS

(a) Model 1

Fuselage:

Effective fineness ratio, $l\sqrt{\frac{\pi}{4A_{\max}}}$	12.52
Total frontal area, sq ft	0.2092
Inlet minimum area, sq ft	0.0358
Inlet capture area, sq ft	0.0484
Duct-exit area, sq ft	0.0400

Wing:

Aspect ratio	3.0
Taper ratio	0.2
Mean aerodynamic chord, ft	1.148
Airfoil section	NACA 65A004
Total plan-form area, sq ft	3.0

Empennage:

Aspect ratio	
Vertical tail	1.5
Horizontal tail	3.0
Taper ratio	0.2
Airfoil section	NACA 65A004
Total plan-form area	
Vertical tail, sq ft	0.615
Horizontal tail, sq ft	0.480

TABLE II
INTERCEPTOR PHYSICAL DIMENSIONS - Continued

(b) Model 2

Fuselage:

Effective fineness ratio, $2\sqrt{\frac{\pi}{4A_{\max}}}$	11.78
Total frontal area, sq ft	0.2365
Inlet minimum area, sq ft	0.0457
Inlet capture area, sq ft	0.0612
Duct-exit area, sq ft	0.0562

Wing:

Aspect ratio	3.0
Taper ratio	0.2
Mean aerodynamic chord, ft	1.299
Airfoil section	NACA 65A004
Total plan-form area, sq ft	3.837

Empennage:

Aspect ratio	
Vertical tail	1.5
Horizontal tail	3.0
Taper ratio	0.2
Airfoil section	NACA 65A004
Total plan-form area	
Vertical tail, sq ft	0.662
Horizontal tail, sq ft	0.614

TABLE II
INTERCEPTOR PHYSICAL DIMENSIONS - Concluded
(c) Model 3

Fuselage:

Effective fineness ratio, $2\sqrt{\frac{\pi}{4A_{\max}}}$	12.62
Total frontal area, sq ft	0.214

Wing:

Aspect ratio	3.0
Taper ratio	0.2
Mean aerodynamic chord, ft	1.148
Airfoil section	NACA 65A004
Total plan-form area, sq ft	3.0

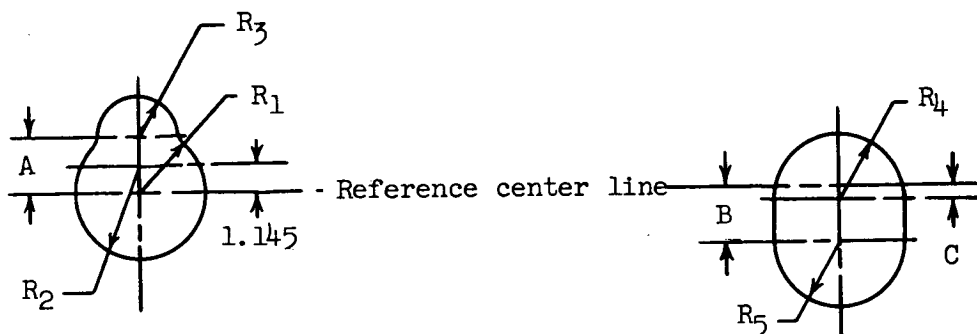
Empennage:

Aspect ratio	
Vertical tail	1.5
Horizontal tail	3.0
Taper ratio	0.2
Airfoil section	NACA 65A004
Total plan-form area	
Vertical tail, sq ft	0.615
Horizontal tail, sq ft	0.480

TABLE III
FUSELAGE ORDINATES

(a) Model 1

[All dimensions in inches. Letter dimensions apply to this table only.]



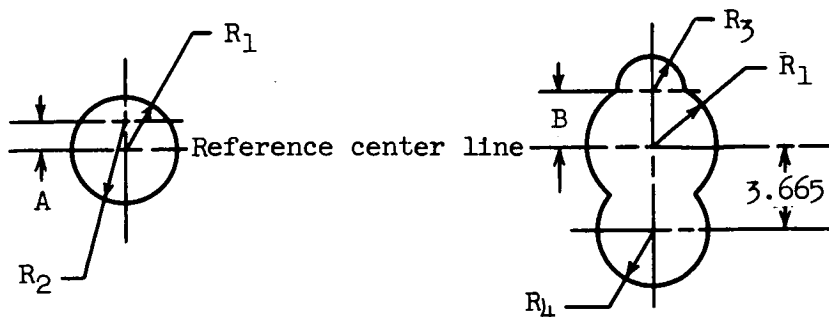
Fuselage station	A	R_1	R_2	R_3	B	C	R_4	R_5
Ref. 0	----	0	----	----	----	----	----	----
5	----	.76	----	----	----	----	----	----
10	----	1.37	----	----	----	----	----	----
15	----	1.87	3.19	----	----	----	----	----
20	2.12	2.22	3.38	0.92	----	----	----	----
25	2.23	2.43	3.49	1.45	----	----	----	----
28	2.28	2.49	3.50	1.35	2.29	----	----	2.00
30	2.32	2.50	3.50	1.23	2.29	----	----	2.12
32.5	2.36	2.50	3.50	.96	2.29	----	----	2.12
35	2.41	2.50	----	.61	2.29	----	----	2.31
40	----	2.50	----	0	2.18	----	----	2.40
45	----	2.50	----	----	2.08	----	----	2.50
50	----	2.50	----	----	2.05	----	----	2.50
55	----	----	----	----	1.92	0.16	2.50	2.50
60	----	----	----	----	1.63	.45	2.50	2.50
65	----	----	----	----	1.28	.80	2.42	2.42
70	----	----	----	----	1.04	1.04	2.25	2.25
75	----	----	----	----	1.14	.94	1.88	1.88
79	----	----	----	----	1.04	1.04	1.46	1.46

TABLE III

FUSELAGE ORDINATES - Continued

(b) Model 2

[All dimensions in inches. Letter dimensions apply to this table only.]

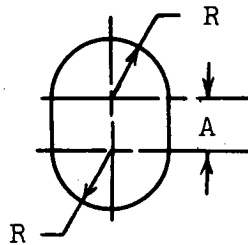


Fuselage station	R_1	A	R_2	B	R_3	R_4
Ref. 0	0	-----	-----	-----	-----	-----
2.050	.424	-----	-----	-----	-----	-----
5.656	1.086	-----	-----	-----	-----	-----
11.312	1.697	-----	-----	-----	-----	-----
14.480	1.946	0.150	1.946	-----	-----	1.674
16.698	2.115	-----	-----	-----	-----	1.912
19.796	2.313	-----	-----	-----	-----	2.014
22.624	2.387	-----	-----	2.353	1.052	2.115
25.452	2.466	-----	-----	2.387	1.584	2.195
28.281	2.511	-----	-----	2.421	1.618	2.285
31.109	2.590	-----	-----	2.466	1.550	2.410
33.937	2.624	-----	-----	2.499	1.369	2.489
36.765	2.658	-----	-----	2.523	1.086	2.500
39.593	2.647	-----	-----	2.557	.679	2.488
42.421	2.636	-----	-----	2.590	.238	2.477
45.249	2.590	-----	-----	-----	-----	2.466
50.905	2.477	-----	-----	-----	-----	2.443
56.561	2.330	-----	-----	-----	-----	2.240
62.217	2.138	-----	-----	-----	-----	1.878
65.611	1.968	-----	-----	-----	-----	1.606
67.873	1.800	-----	-----	-----	-----	-----
73.529	1.199	-----	-----	-----	-----	-----
79.185	.777	-----	-----	-----	-----	-----

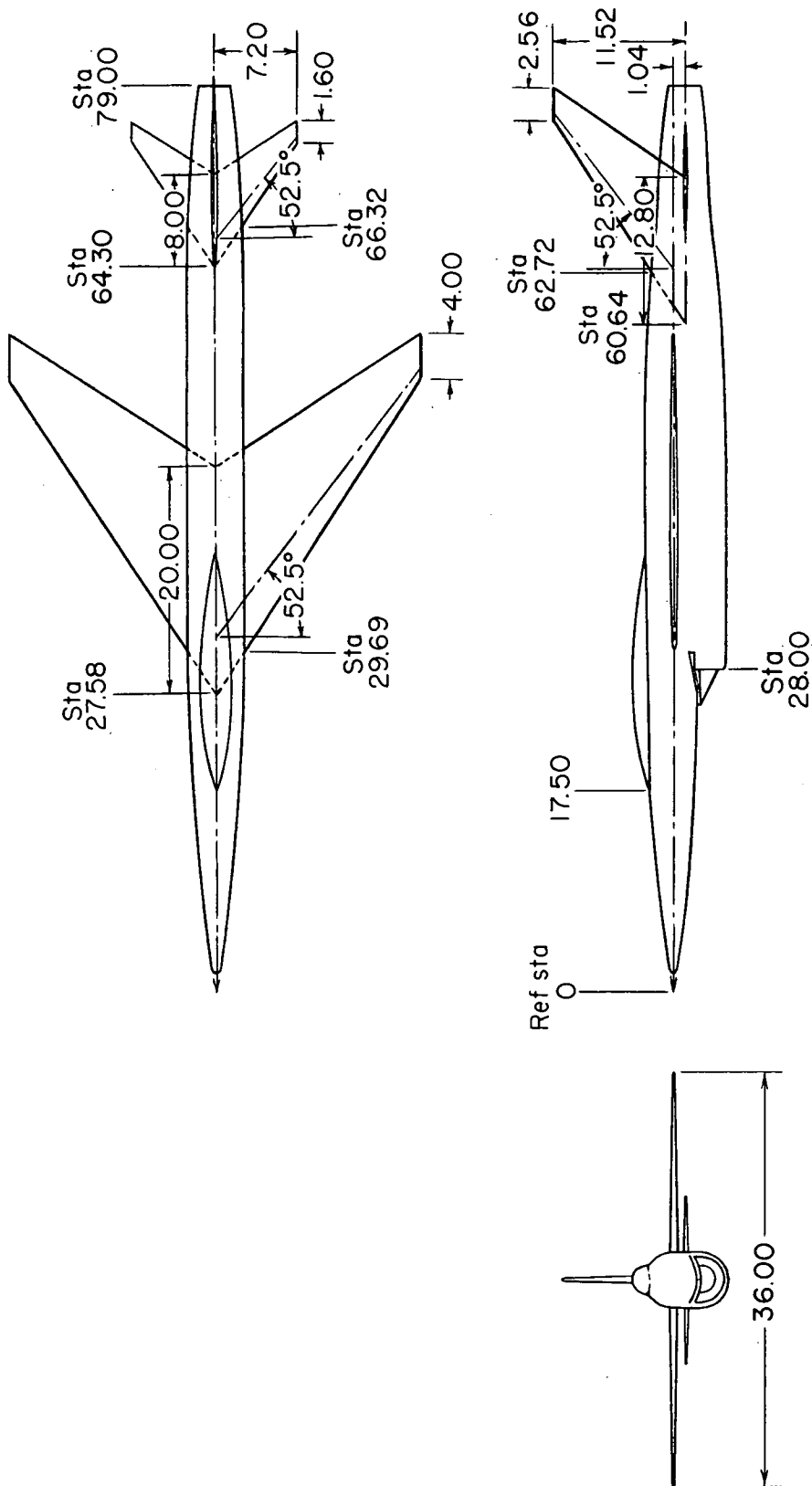
TABLE III
FUSELAGE ORDINATES - Concluded

(c) Model 3

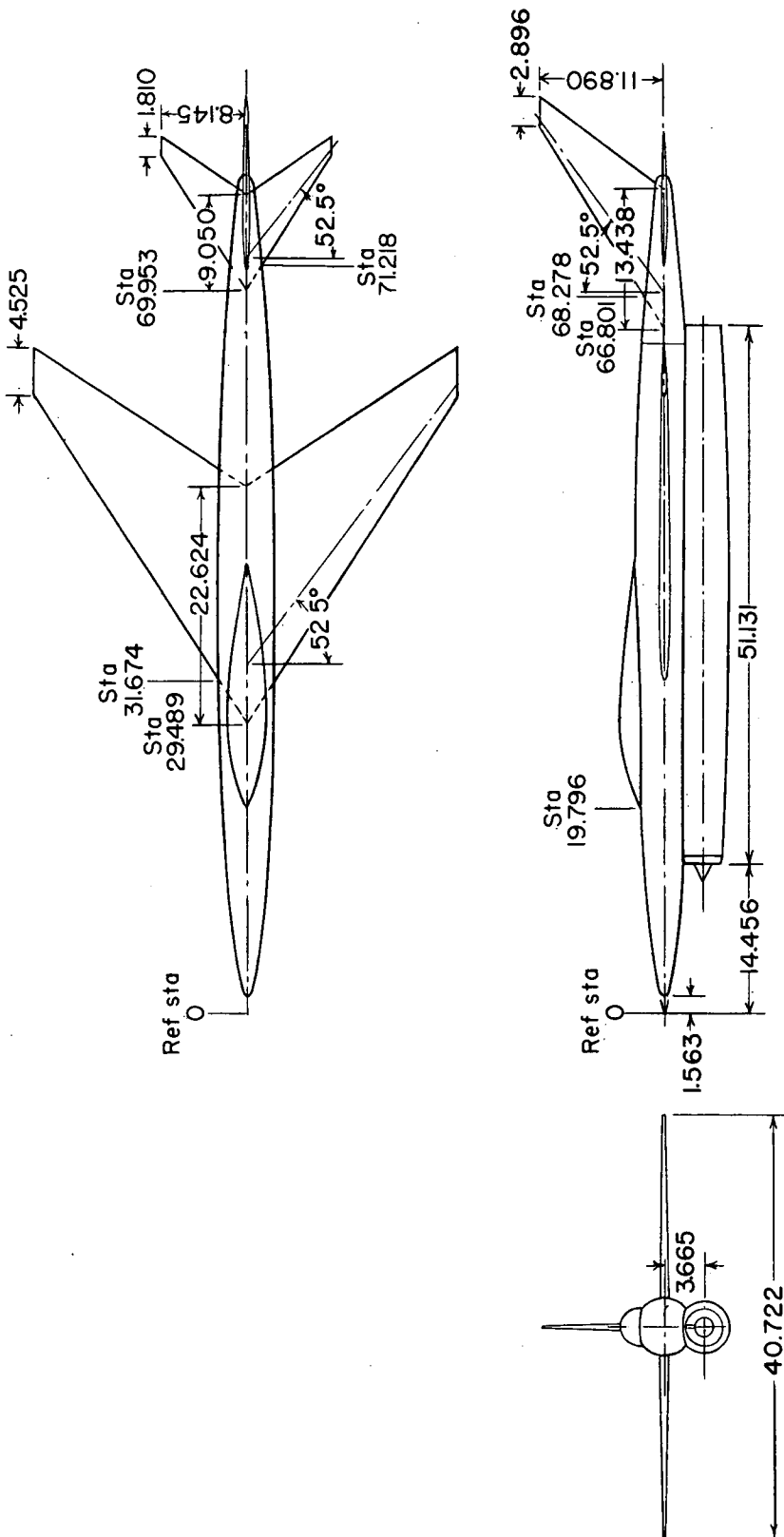
[All dimensions in inches. Letter dimensions apply only to this table.]



Fuselage station	A	R
0	-----	0
5	-----	1.150
10	-----	1.820
15	-----	2.445
20	0.225	2.710
25	.910	2.500
30	1.005	2.500
35	1.110	2.500
40	1.115	2.500
45	1.125	2.500
50	1.050	2.500
55	.935	2.500
60	.755	2.500
65	.410	2.500
70	.040	2.960
75	-----	2.000
79	-----	1.969

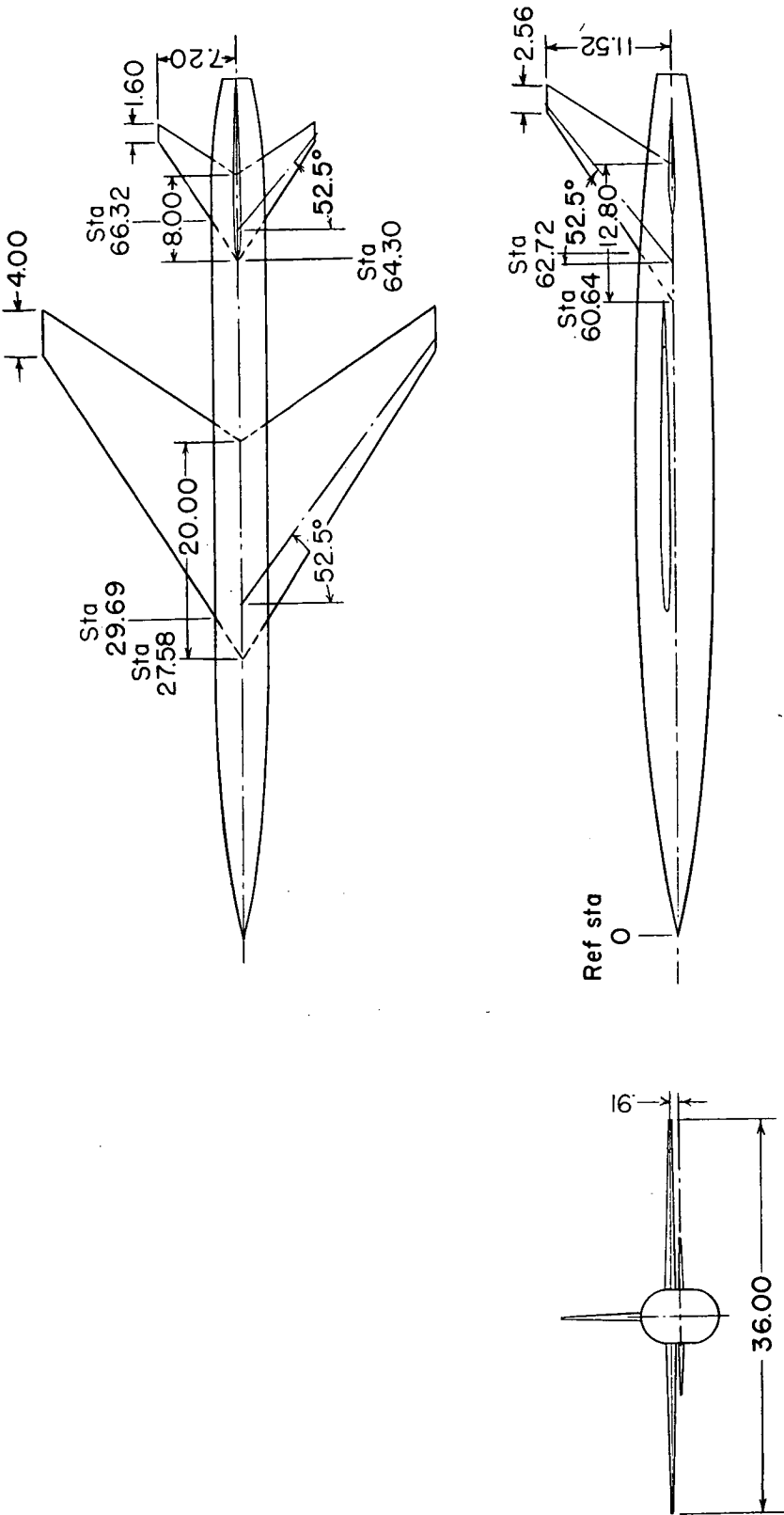


(a) Model 1. Half-conical spike inlet under fuselage.
 Figure 1.- Three-view drawings of rocket-propelled models. All dimensions are in inches.



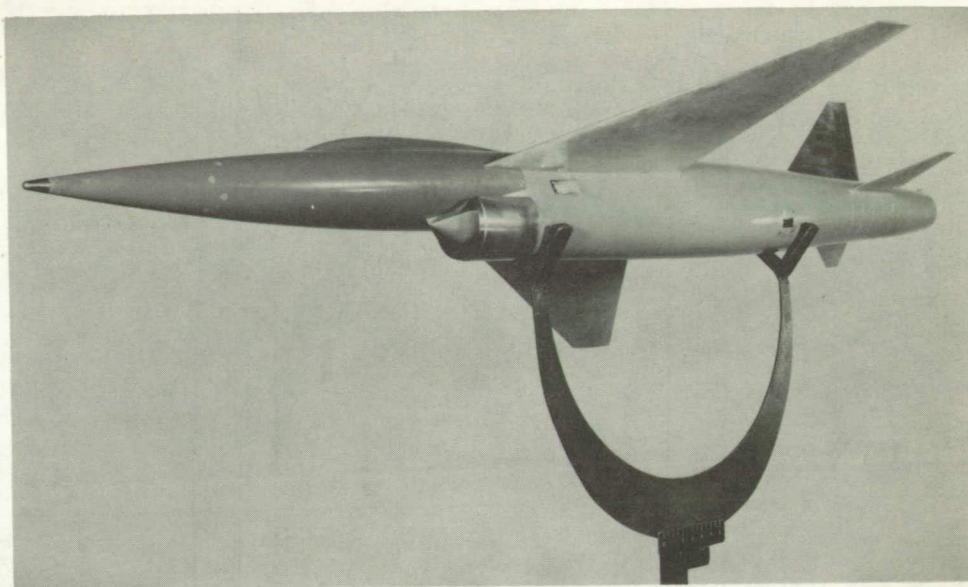
(b) Model 2. Full-conical spike inlet with engine in pod under fuselage.

Figure 1.- Continued.



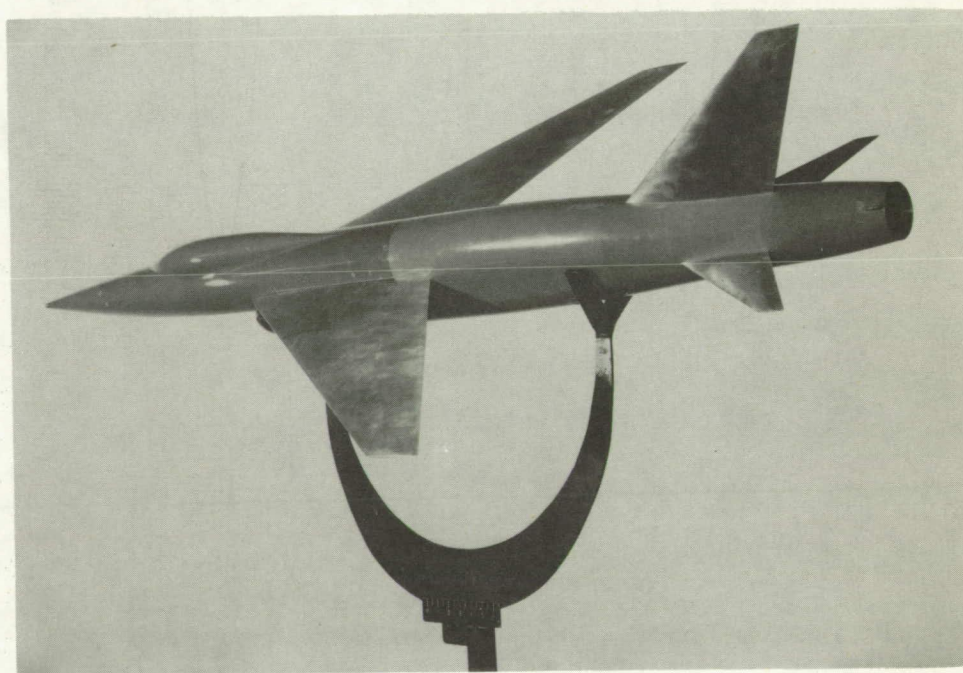
(c) Model 3. Model with faired fuselage.

Figure 1.- Concluded.



(a) Front view of model 1.

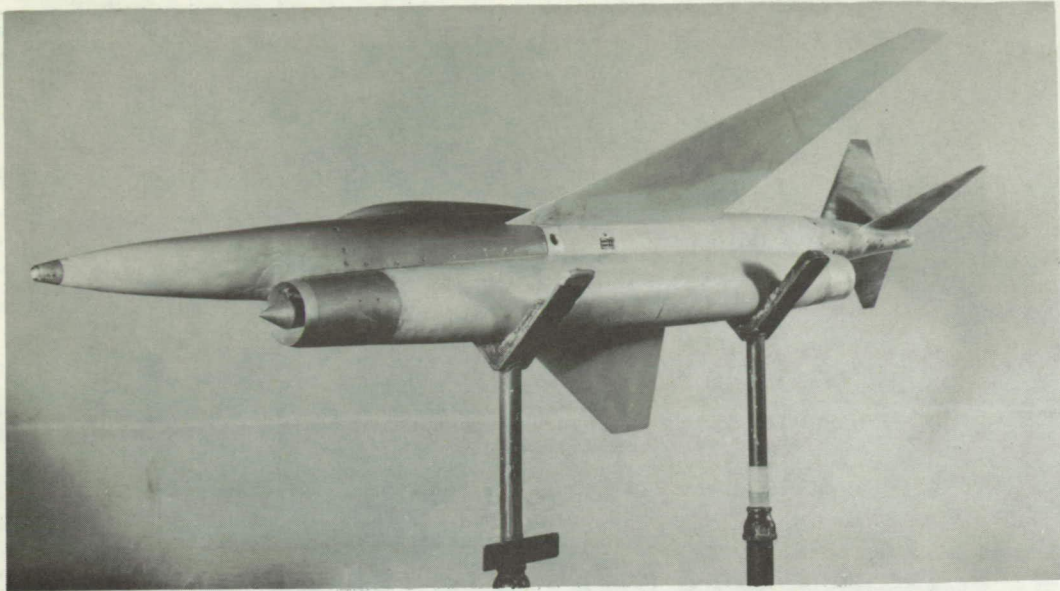
L-83590.1



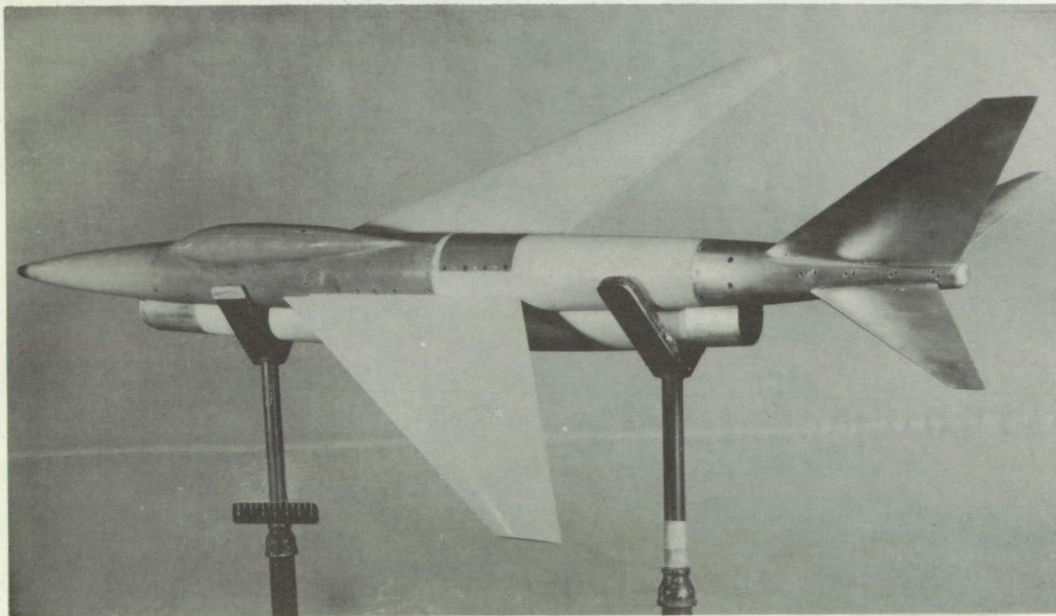
(b) Rear view of model 1.

L-83588.1

Figure 2.- Photographs of rocket-propelled models.

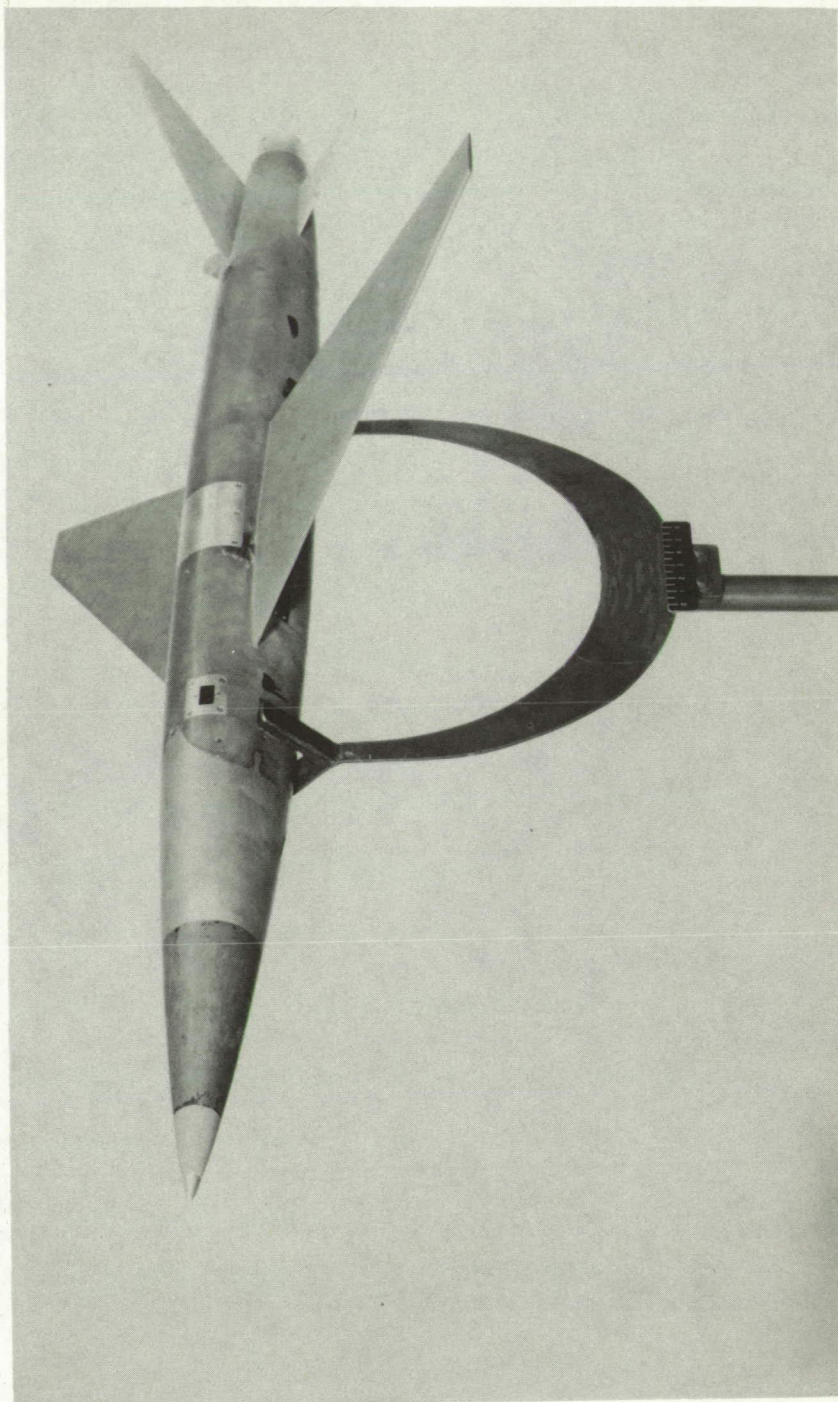


(c) Front view of model 2. L-85096.1



(d) Rear view of model 2. L-85095.1

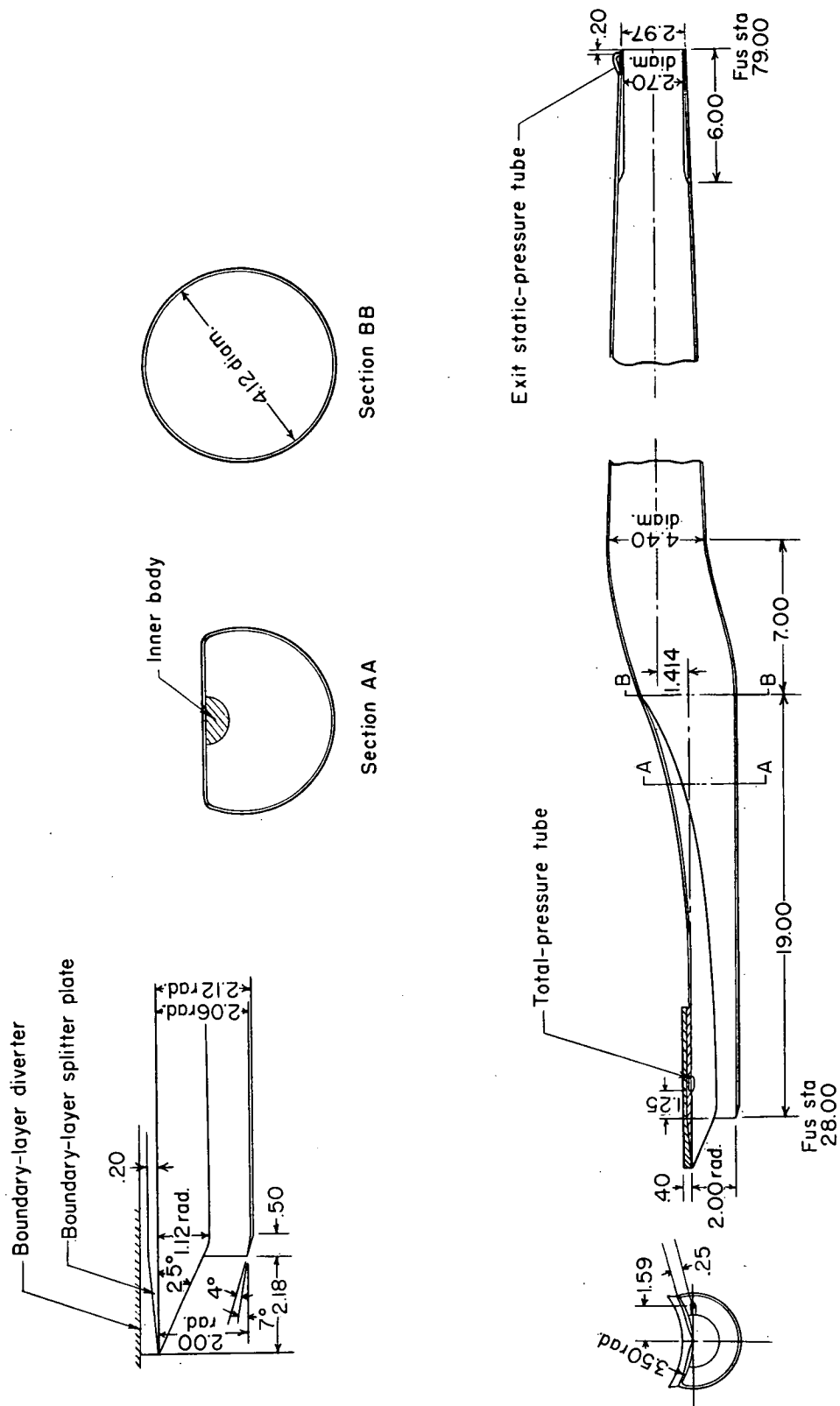
Figure 2.- Continued.



(e) Front view of model 3.

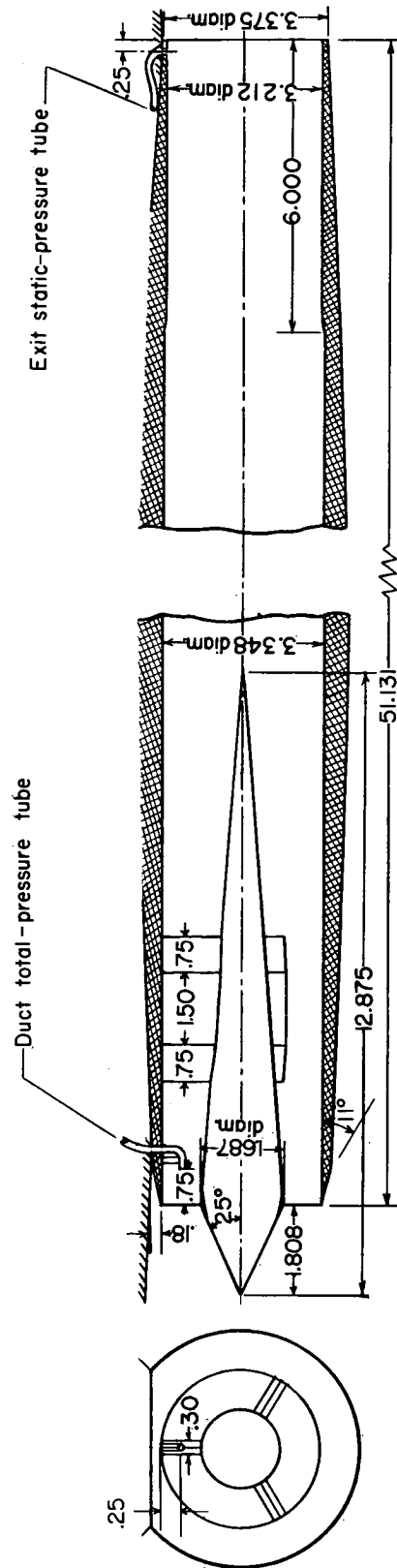
L-82530.1

Figure 2.- Concluded.



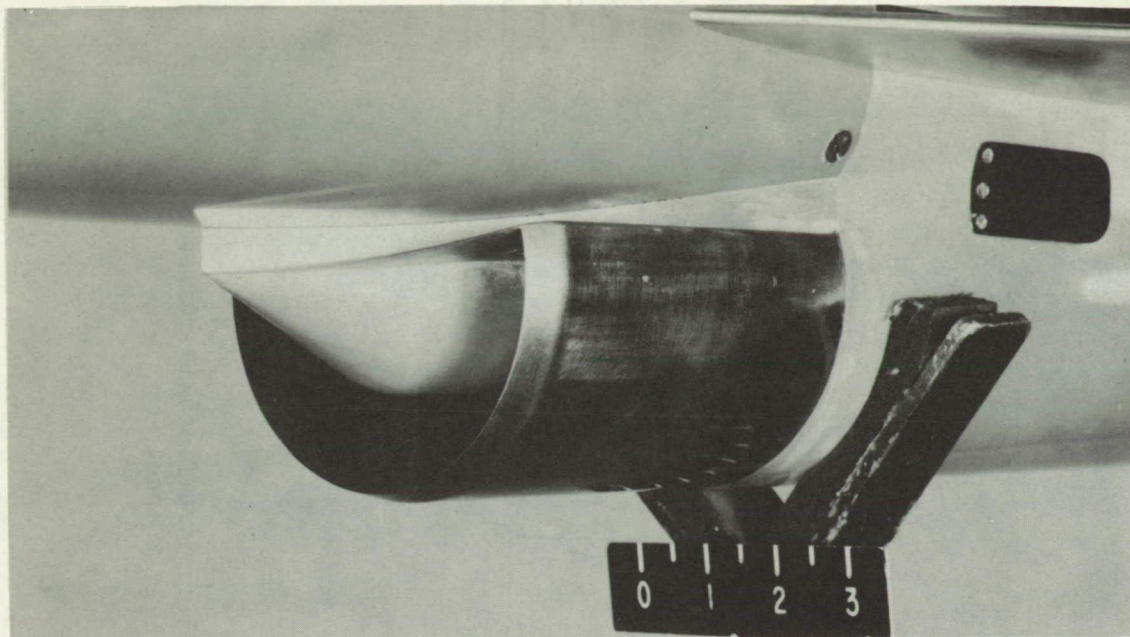
(a) Model 1.

Figure 3.- Details of duct and inlet. All dimensions are in inches.



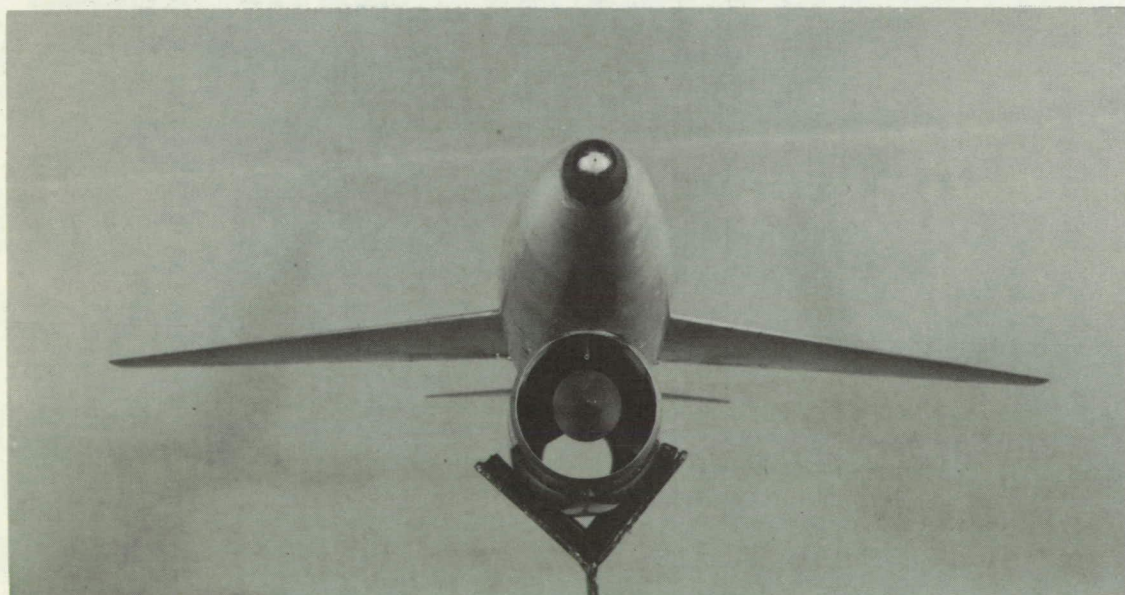
(b) Model 2.

Figure 3.- Concluded.



(a) Model 1.

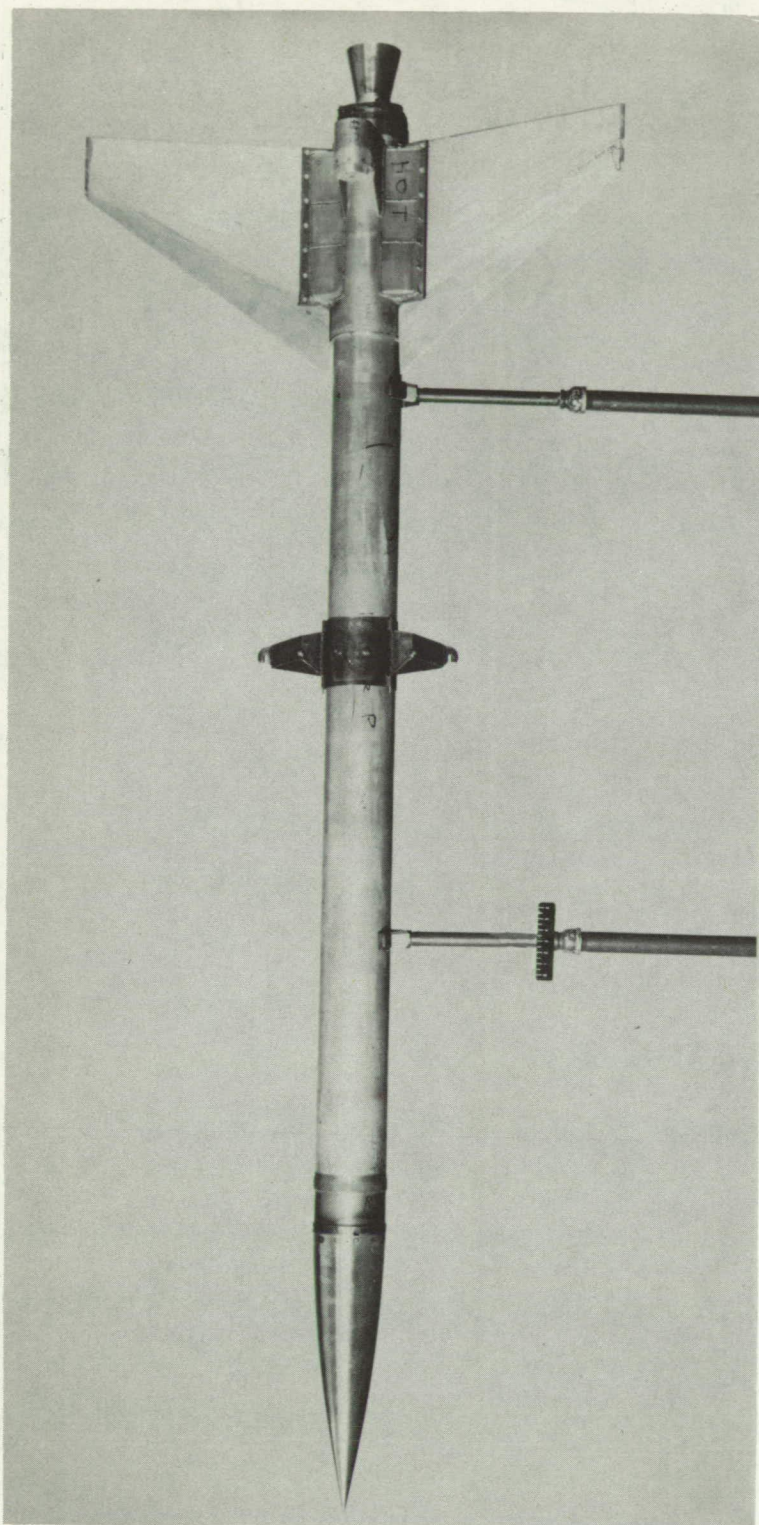
L-83539



(b) Model 2.

L-85093

Figure 4.- Photographs of interceptor inlets.

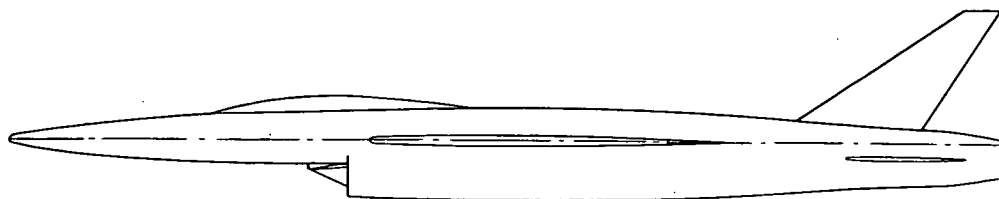


L-82533.1
Figure 6.- Top view of booster with forward support struts in down position.

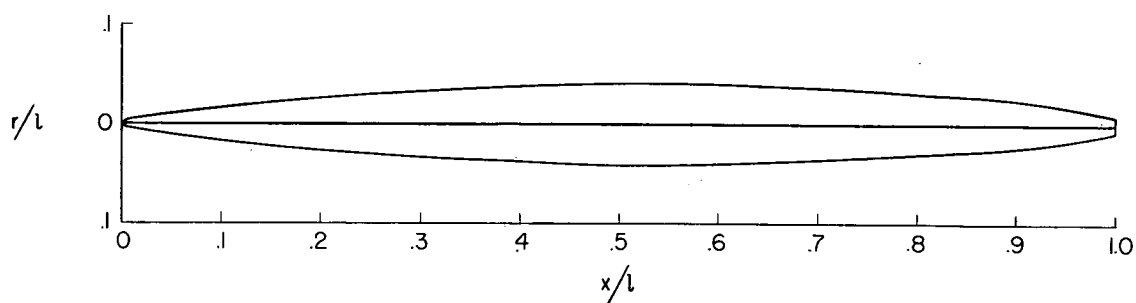


L-82839.1

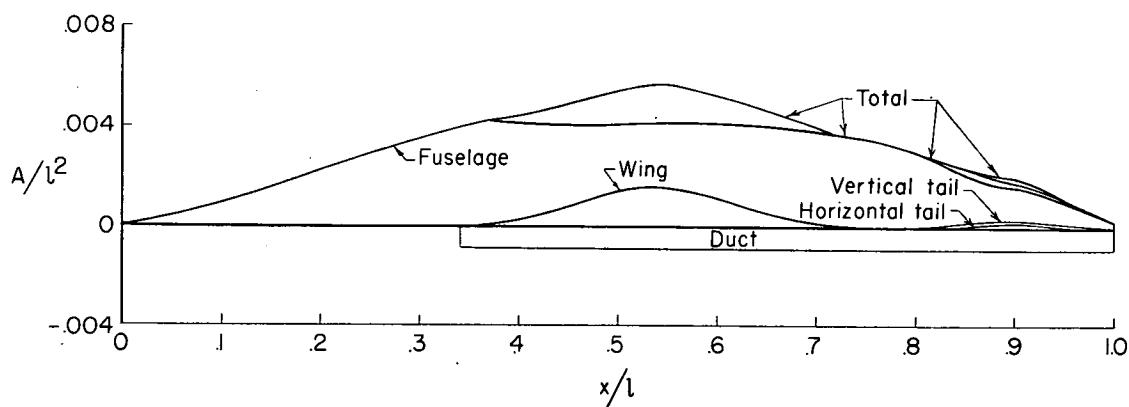
Figure 7.- Model 3 with booster on mobile launcher.



Elevation view of model I



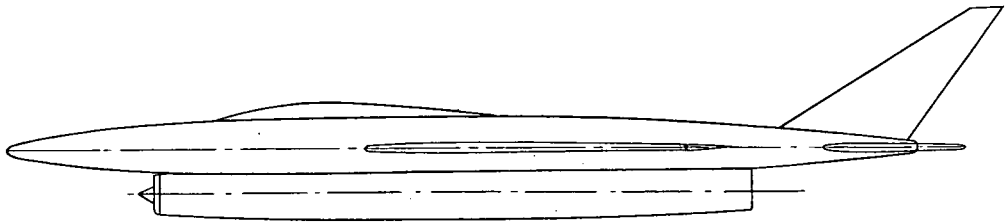
Equivalent body of revolution. Fineness ratio, 11.83.



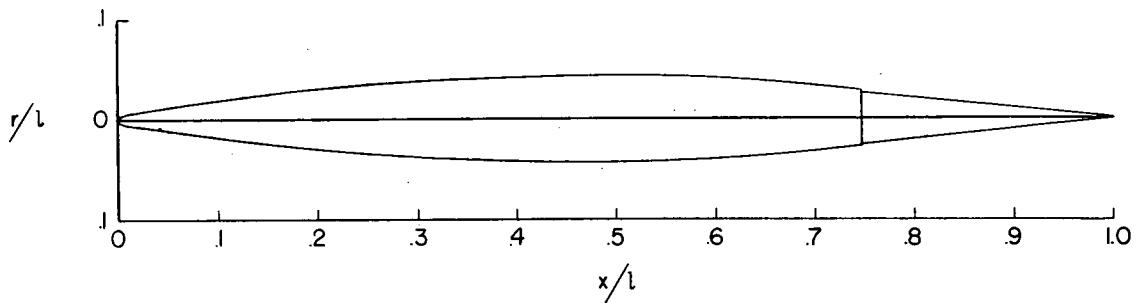
Cross-sectional-area distribution

(a) Model 1.

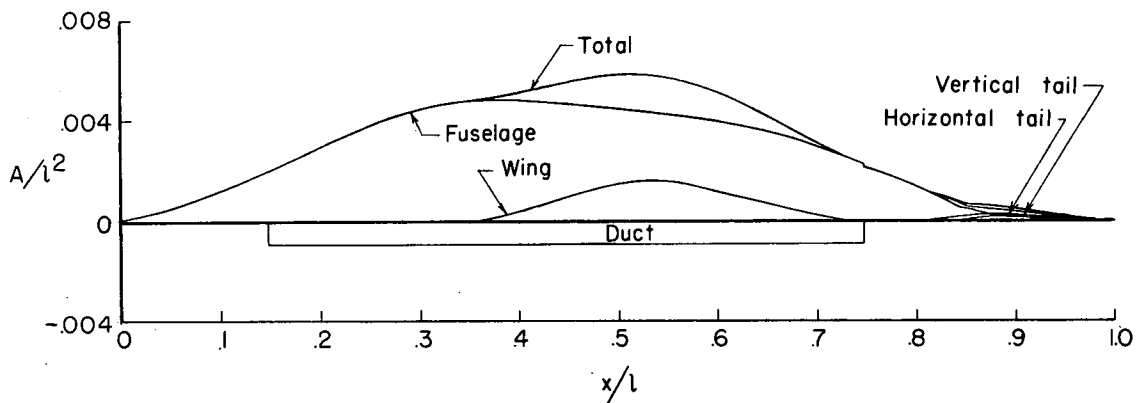
Figure 8.- Area distributions and equivalent bodies of revolution for rocket-propelled models.



Elevation view of model 2



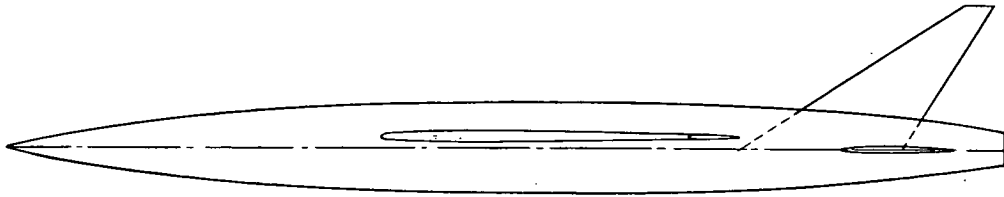
Equivalent body of revolution. Fineness ratio, 11.37.



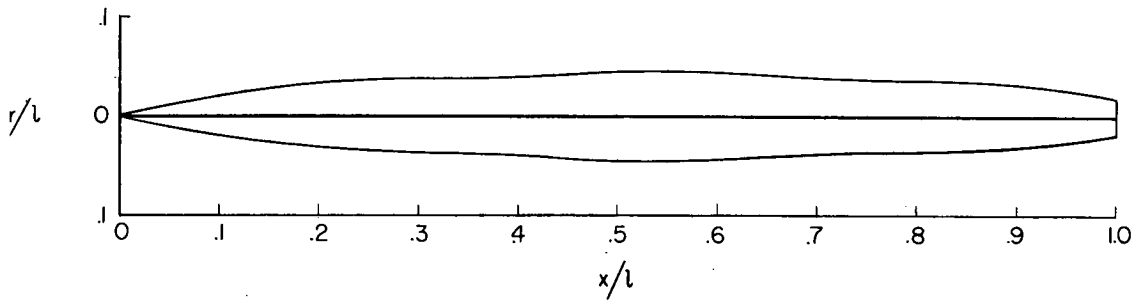
Cross-sectional-area distribution

(b) Model 2.

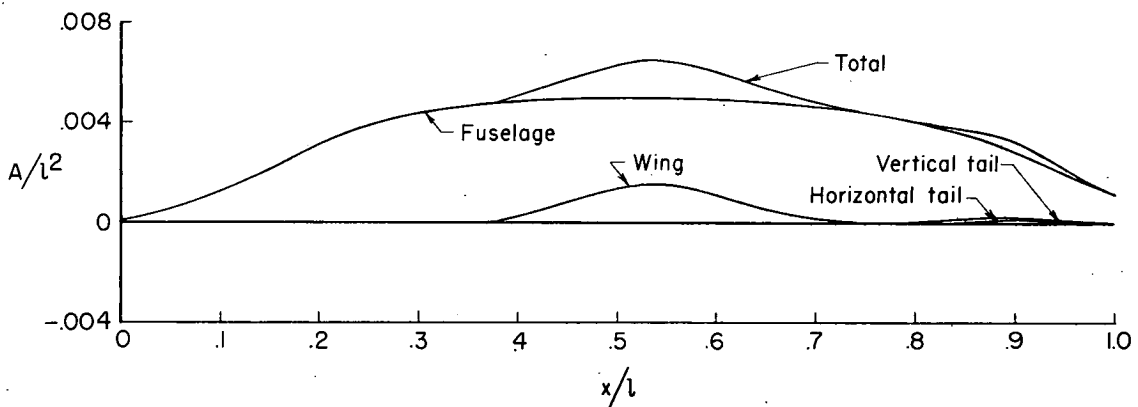
Figure 8.- Continued.



Elevation view of model 3



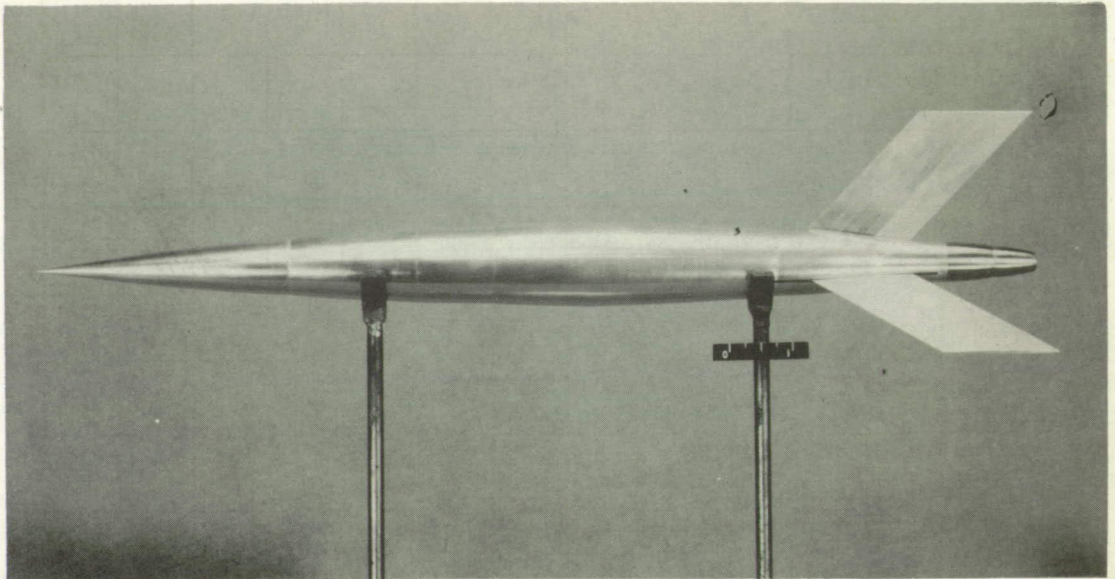
Equivalent body of revolution. Fineness ratio, 10.86.



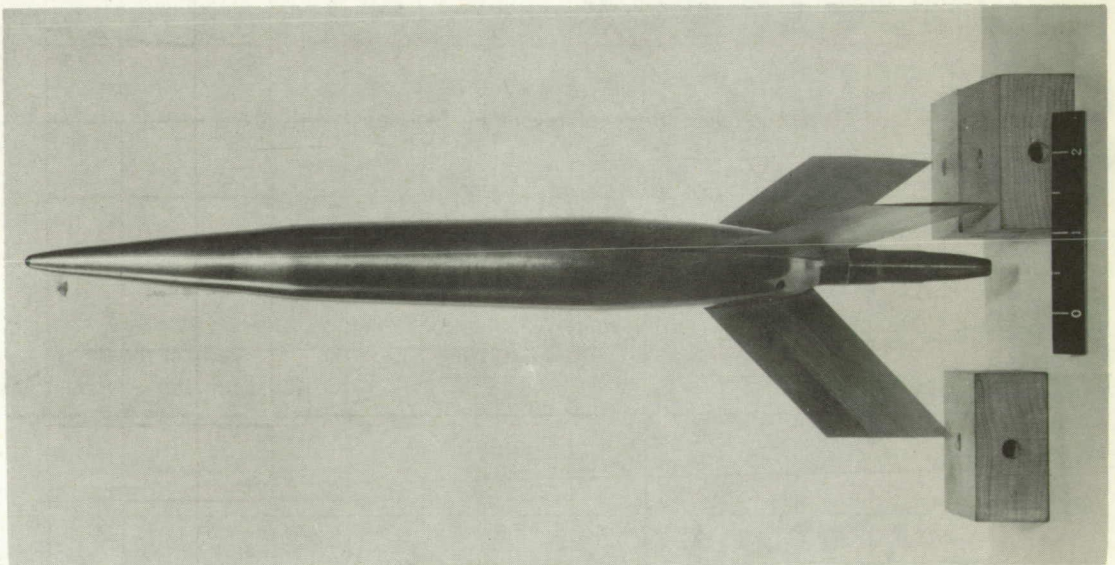
Cross-sectional-area distribution

(c) Model 3.

Figure 8.- Concluded.



(a) Equivalent body for model 1. L-80322



(b) Equivalent body for model 2. L-81980

Figure 9.- One-fifth-scale models with cross-sectional-area distributions of interceptor configurations.

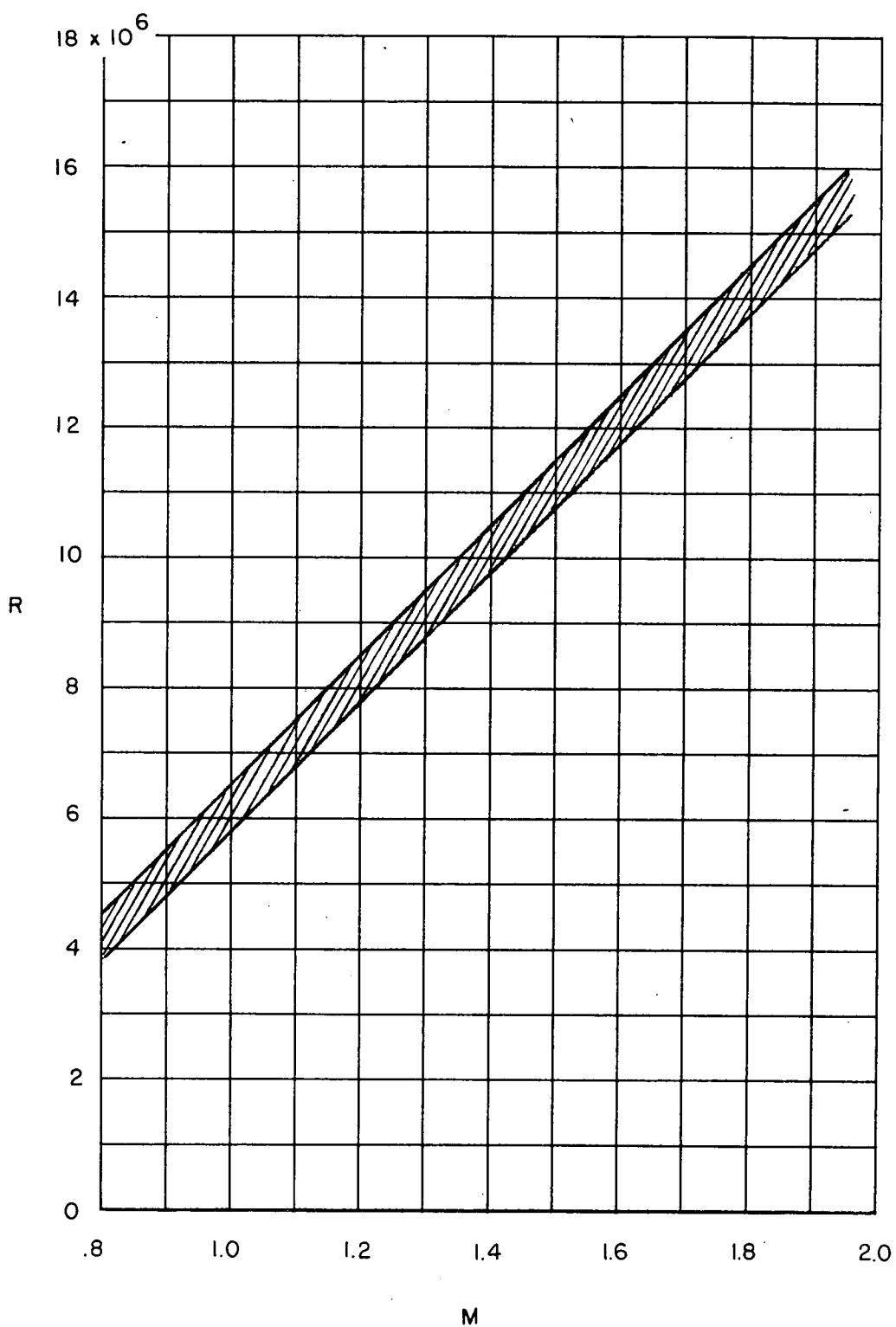
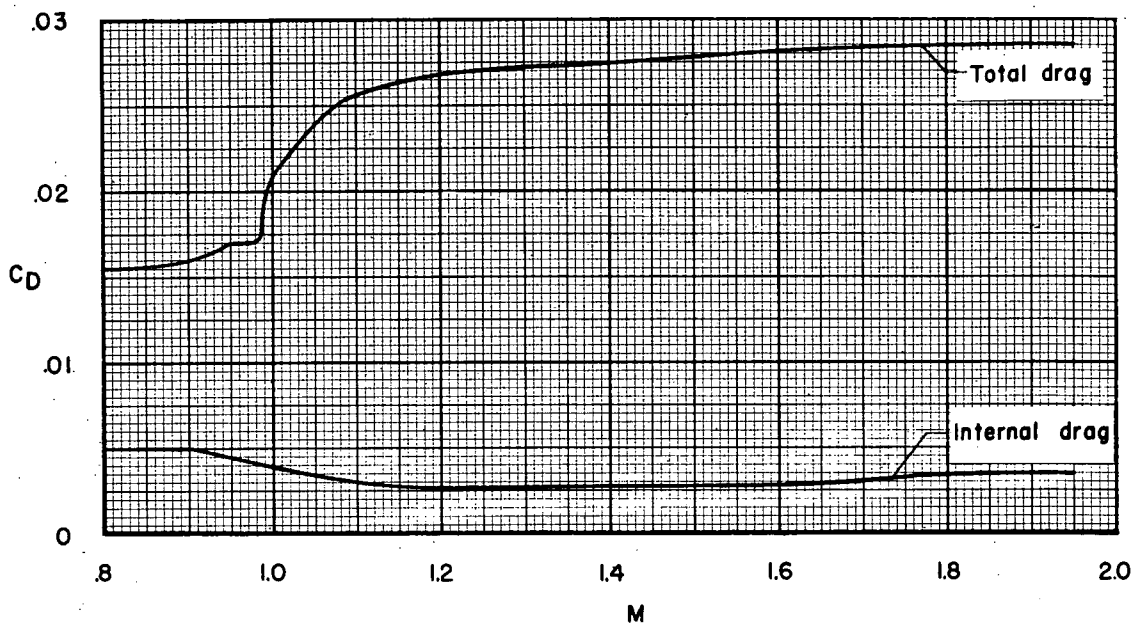
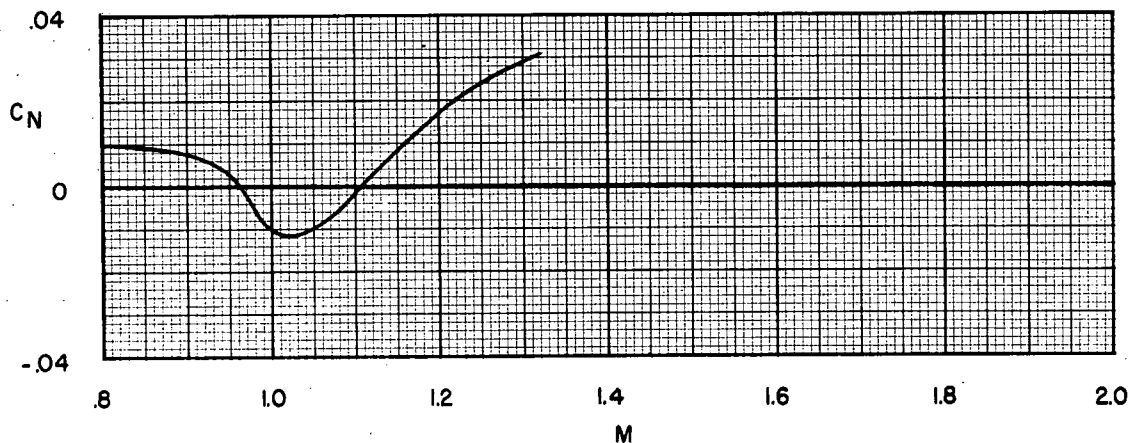


Figure 10.- Variation of Reynolds number, based on wing mean aerodynamic chord, with Mach number for rocket-propelled models.

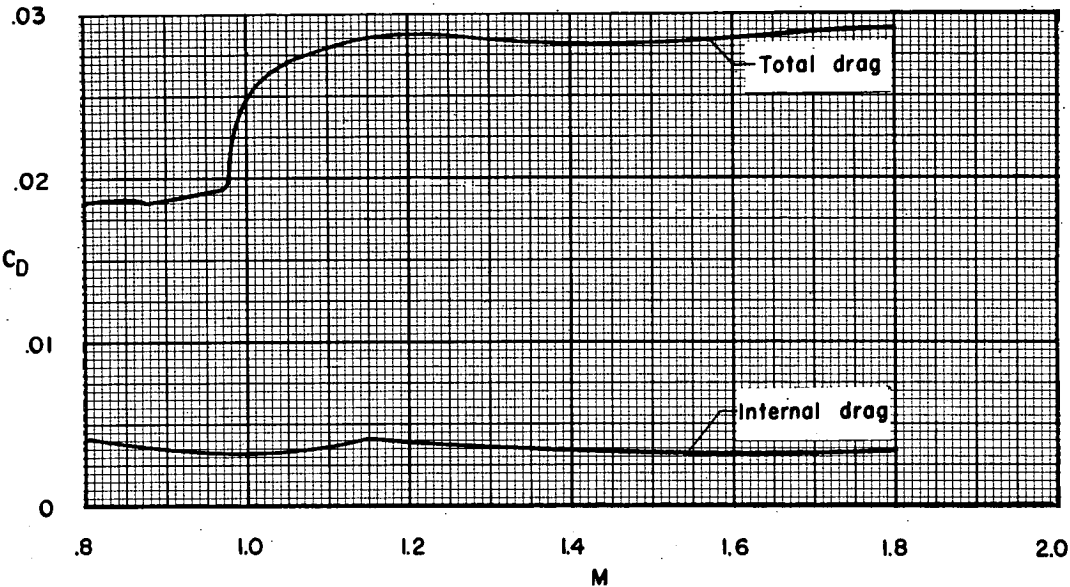


(a) Variation of drag coefficient with Mach number.

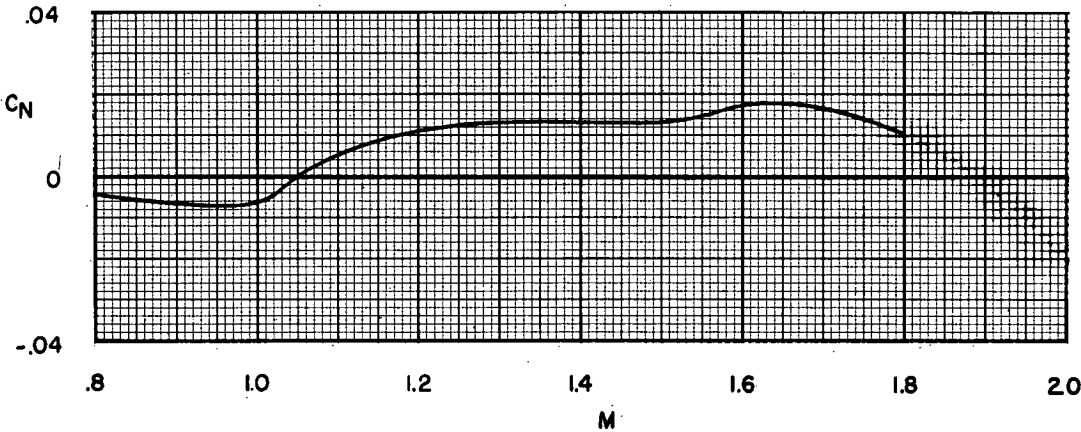


(b) Variation of normal-force coefficient with Mach number.

Figure 11.- Drag and normal-force coefficients for model 1.



(a) Variation of drag coefficient with Mach number.



(b) Variation of normal-force coefficient with Mach number.

Figure 12.- Drag and normal-force coefficients for model 2.

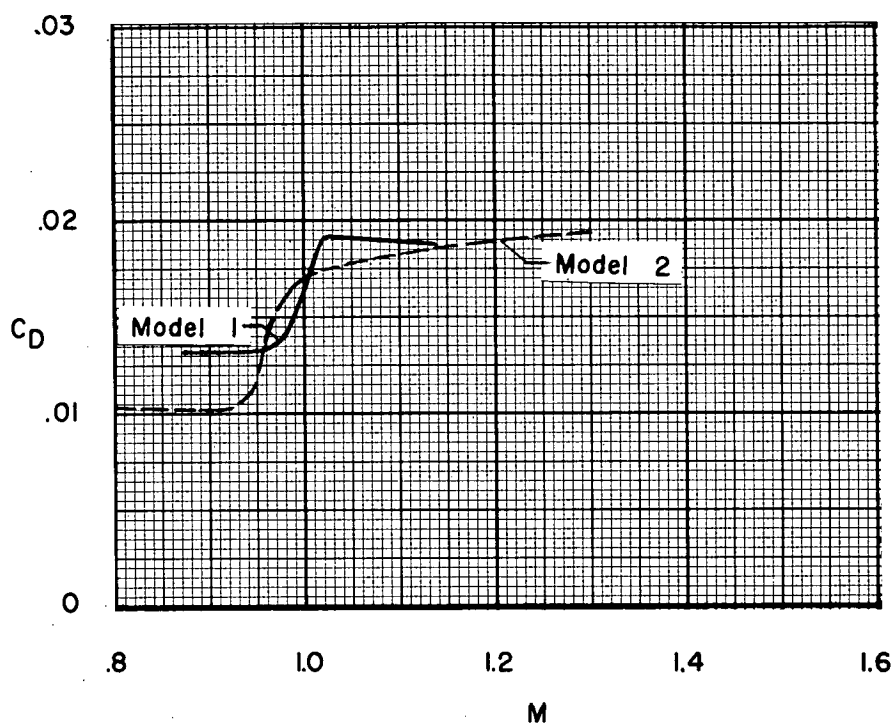


Figure 13.- Drag coefficients of bodies of revolution with same cross-sectional-area distributions as interceptor configurations.

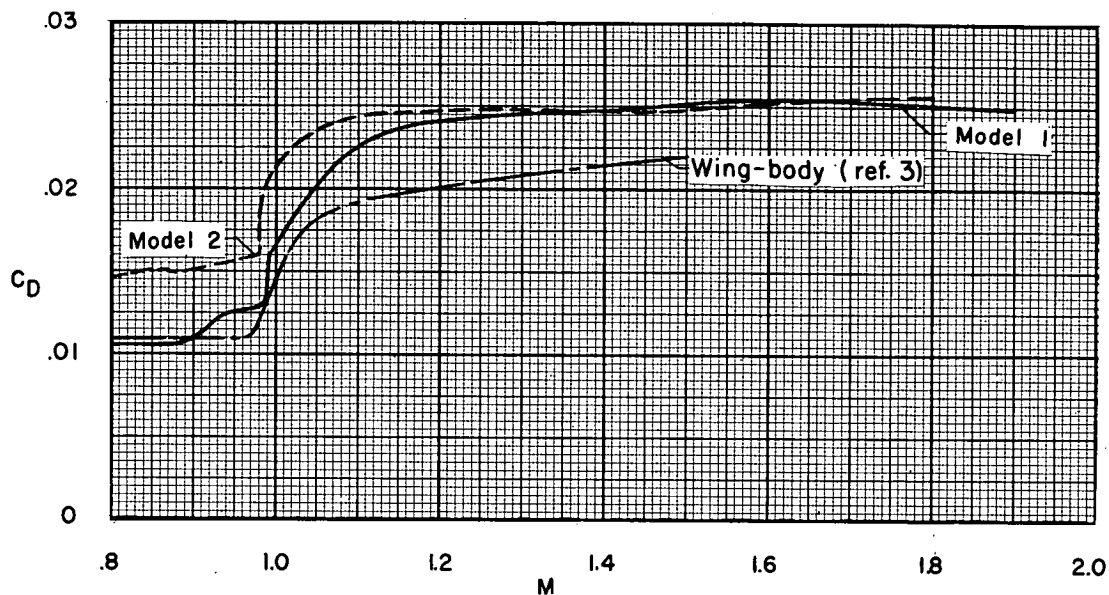


Figure 14.- Comparison of external drag coefficients of interceptor configurations.

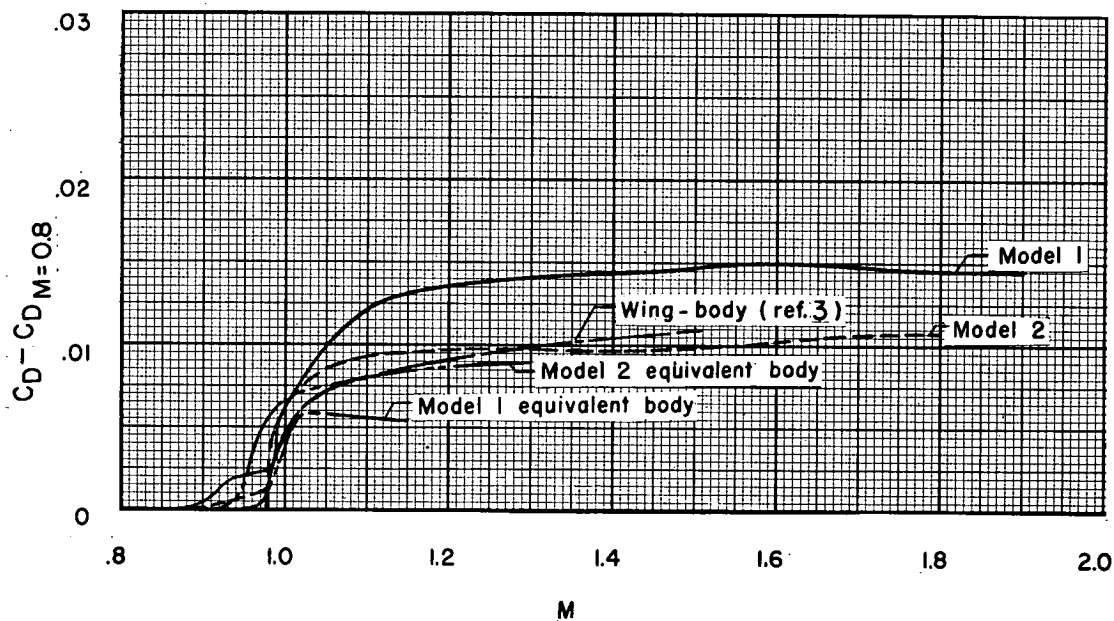
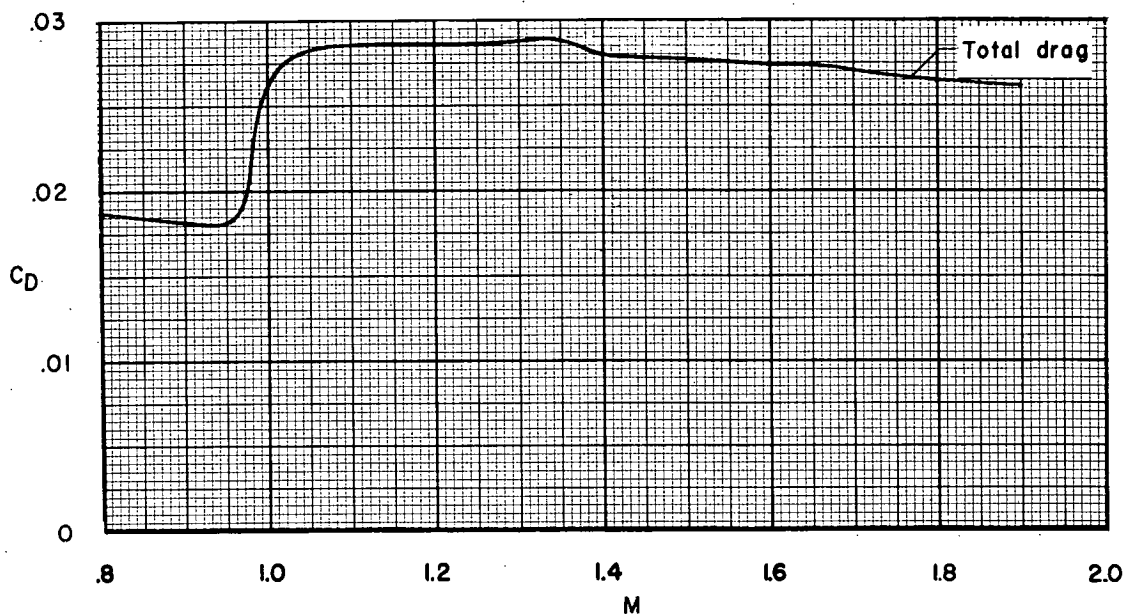
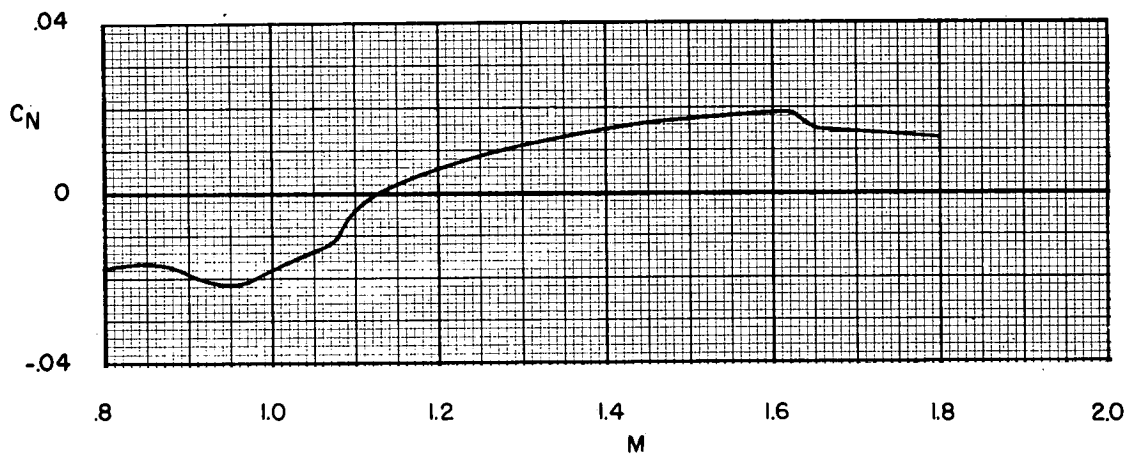


Figure 15.- Comparison of pressure-drag coefficients of interceptor configurations.



(a) Variation of drag coefficient with Mach number.



(b) Variation of normal-force coefficient with Mach number.

Figure 16.- Drag and normal-force coefficients for model 3.

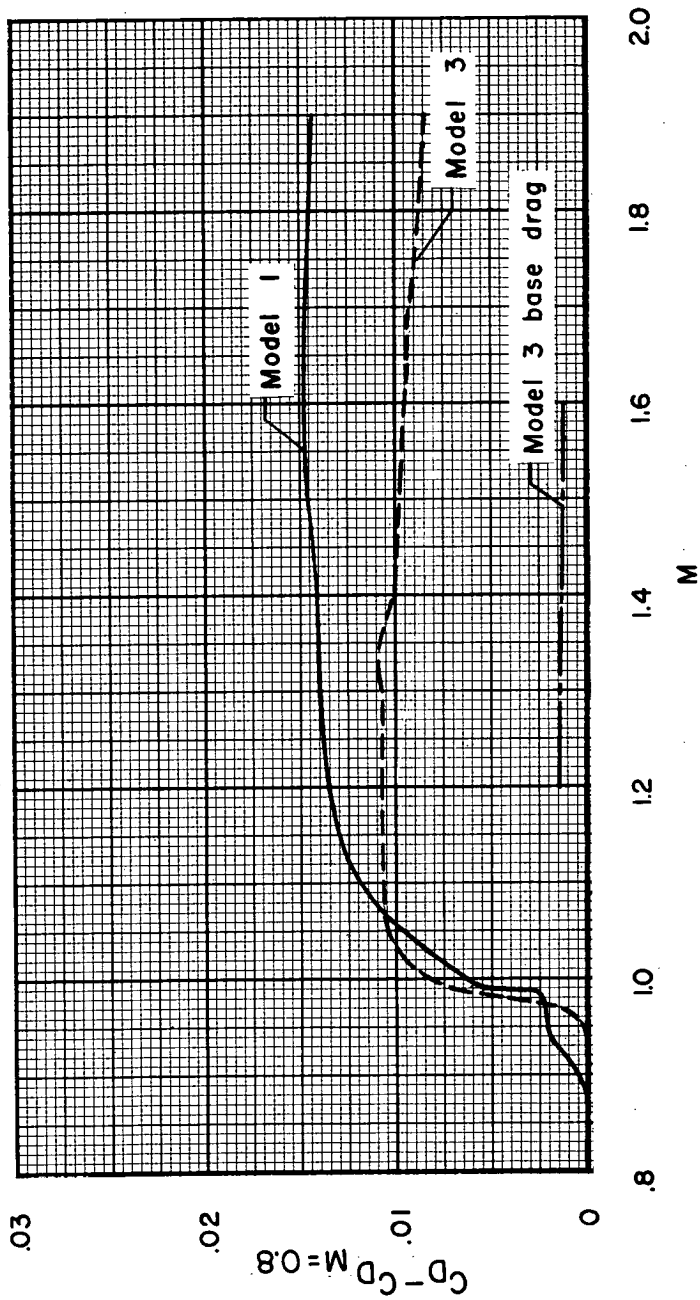
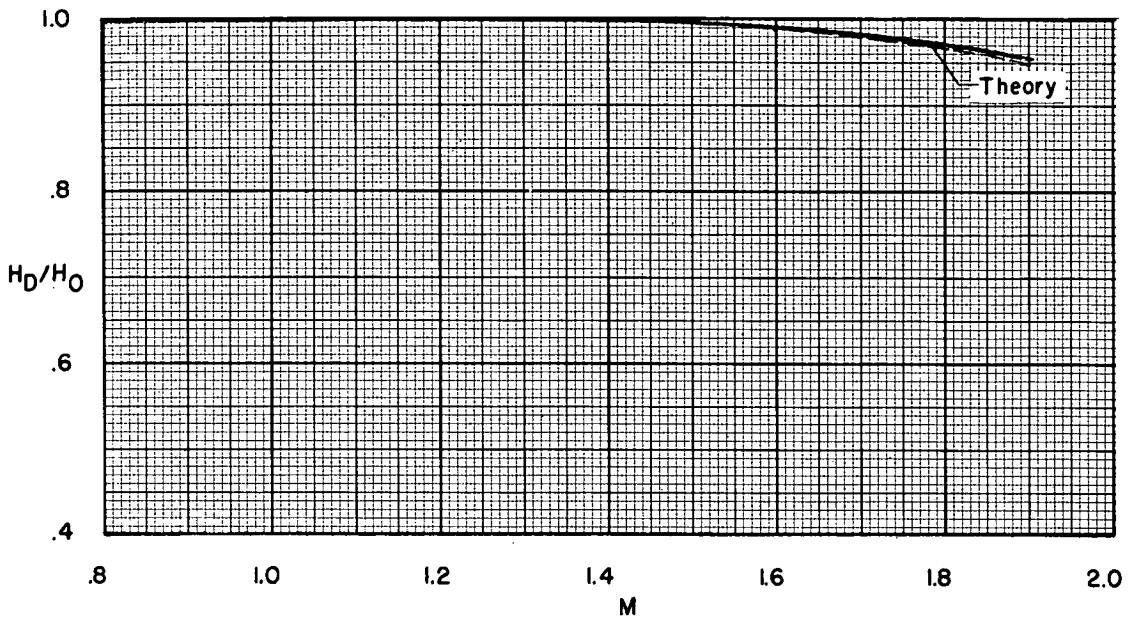
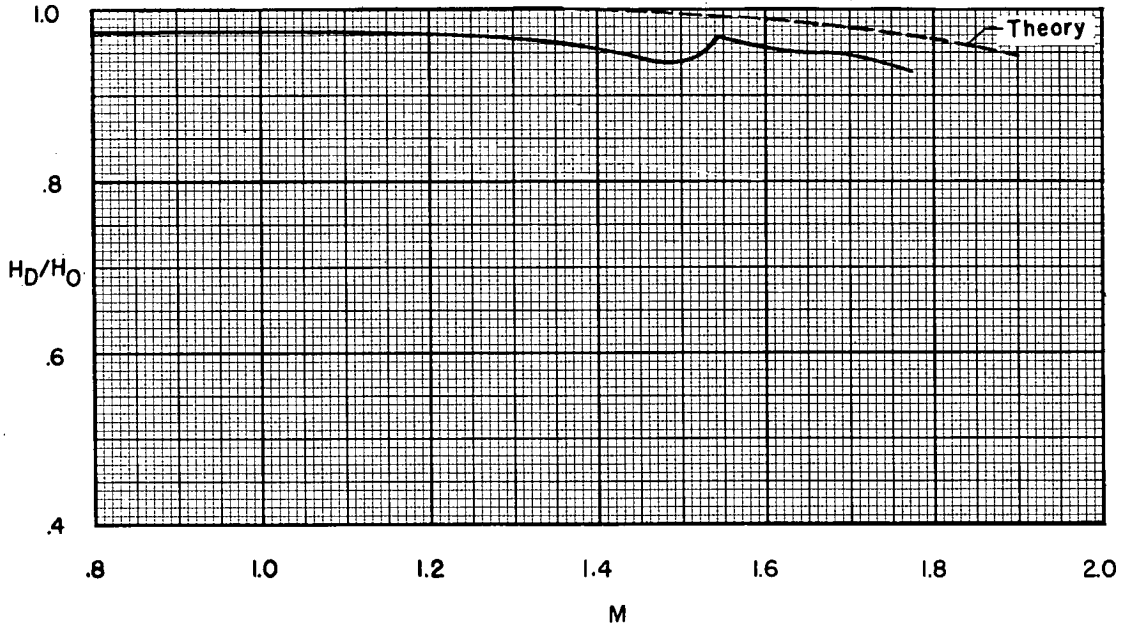


Figure 17.- Comparison of pressure-drag coefficients of models 1 and 3.

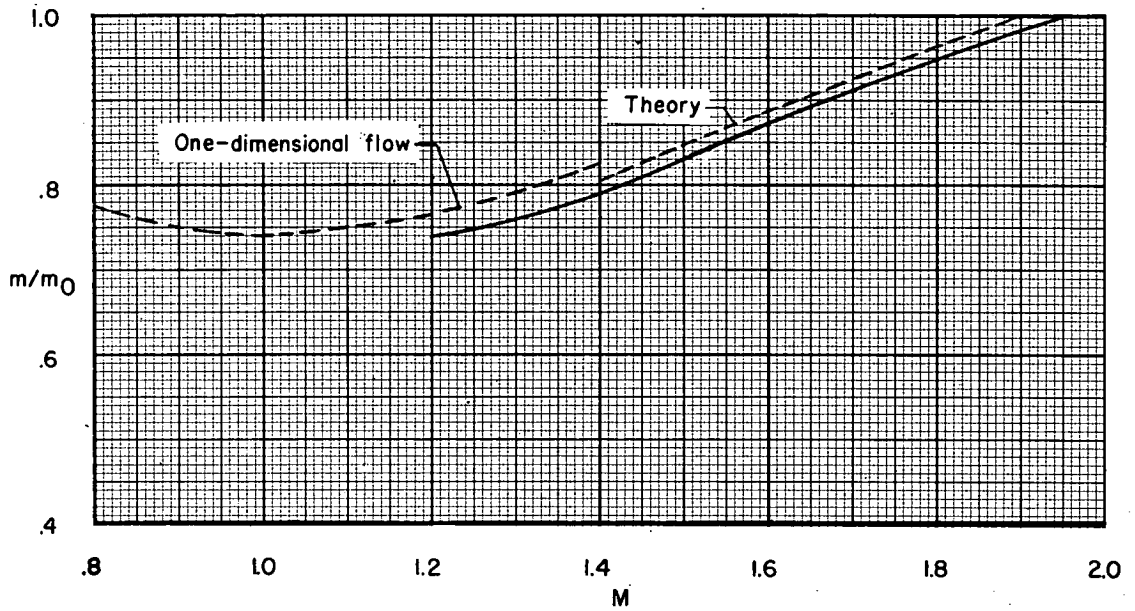


(a) Inlet total-pressure ratio adjacent to fuselage for model 1.

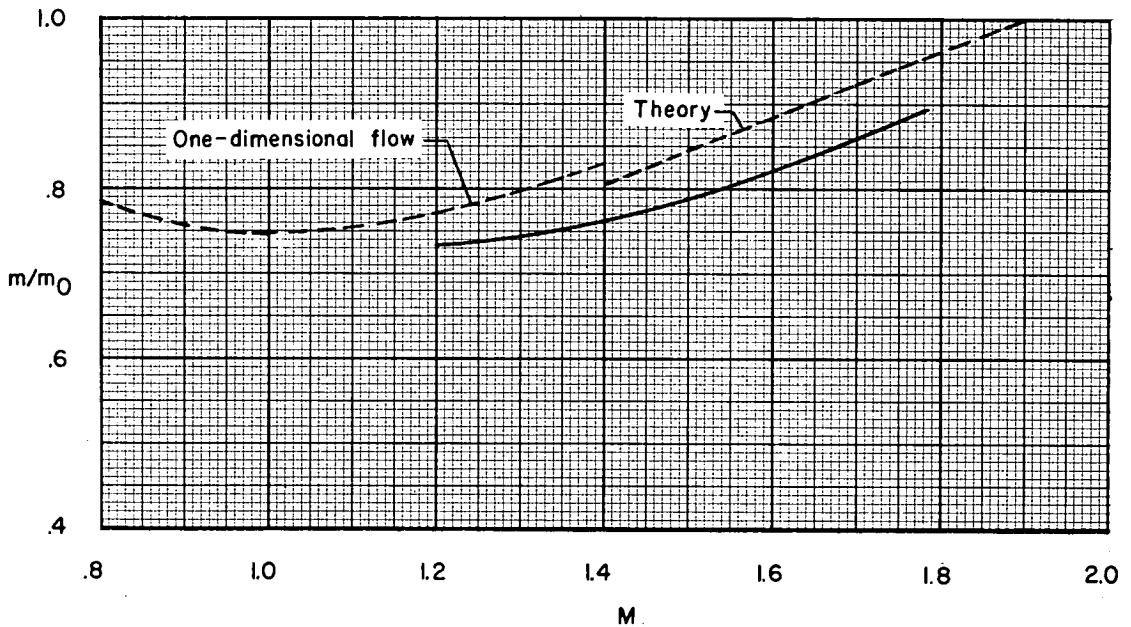


(b) Inlet total-pressure ratio adjacent to fuselage for model 2.

Figure 18.- Variation of inlet total-pressure ratio for interceptor configurations.



(a) Inlet mass-flow ratio for model 1.



(b) Inlet mass-flow ratio for model 2.

Figure 19.- Variation of inlet mass-flow ratio for interceptor configurations.

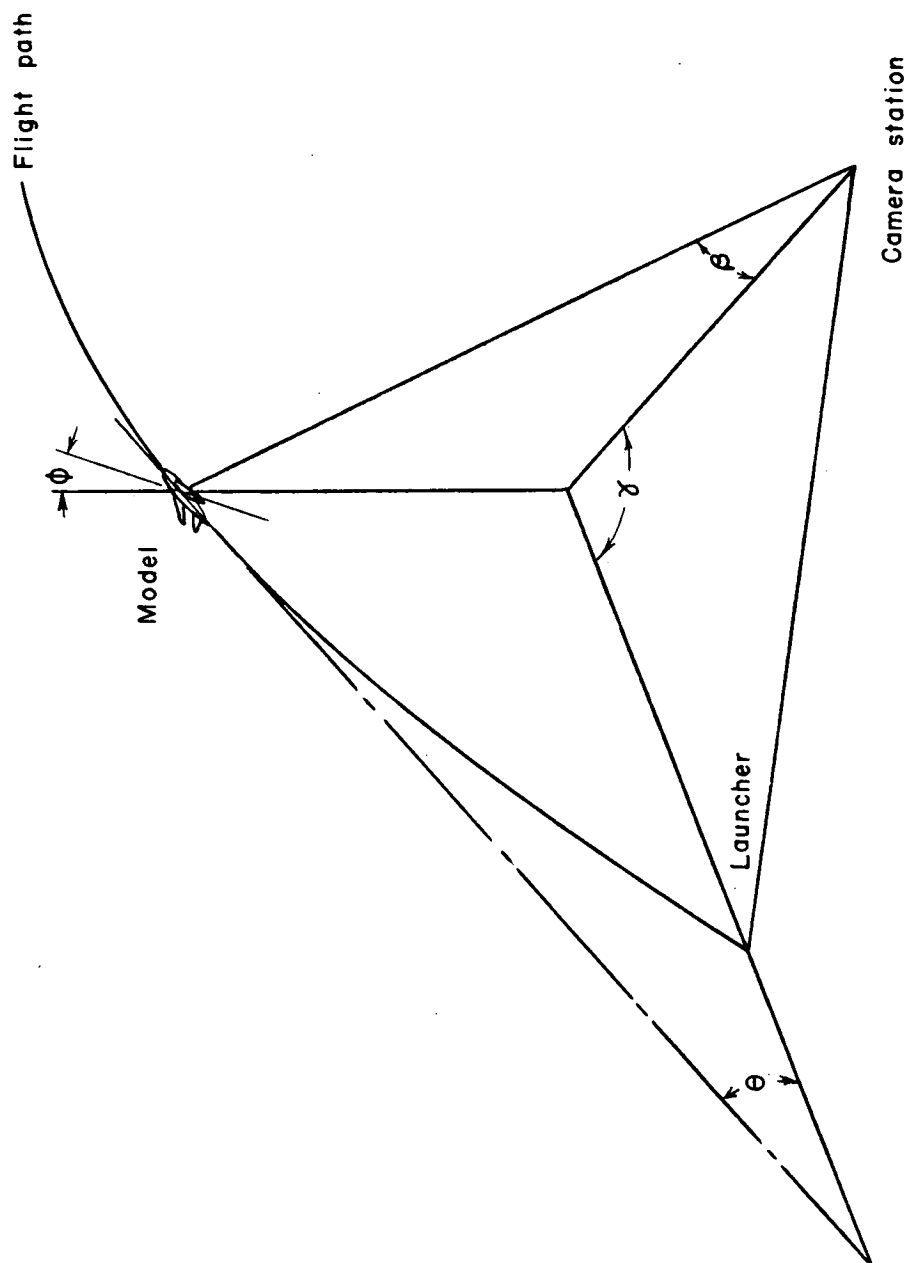


Figure 20.- Spatial relations of model and tracking camera.

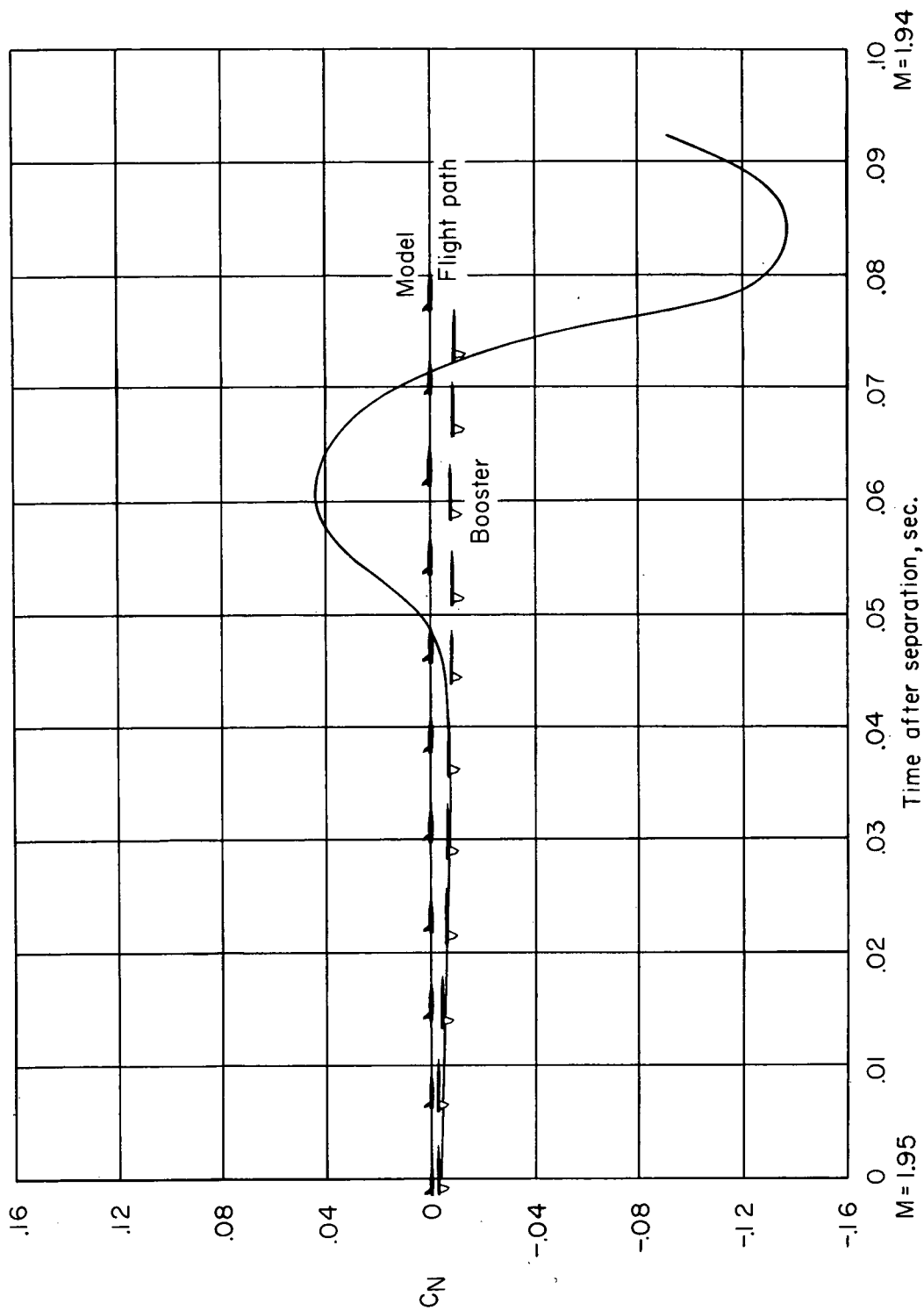


Figure 21.- Model and booster location and model normal-force coefficients during separation.